

Local real space operators for translating Stokes Q/U to E/B maps on the sphere

Aditya Rotti and Kevin Huffenberger

Department of Physics, Florida State University, Keen Physics Building, 77 Chieftan Way, Tallahassee, Florida, U.S.A.

E-mail: adityarotti@gmail.com, khuffenberger@fsu.edu

Abstract. We derive real space operators to translate Stokes Q/U to coordinate independent even and odd parity E/B fields on the sphere and demonstrate their numerical equivalence to the harmonic space methods. In process we also derive real space operators which allow direct decomposition of measured Q/U into Q/U fields corresponding to E-modes and B-modes respectively. These operators are derived on the sphere and account for the curvature effects. The analytical derivations reveal a functional form for the radial kernel, which quantifies the non-local nature of the E and B fields. These real space operators allow the computation of E and B field in each pixel by integrating in a small region around it, and hence it can be easily parallelized and is not memory intensive. A major drawback of these real space operators is that they cannot reliably construct modes on large angular scales $\ell < 50$ with ease. Finally, this study motivates the construction of more locally defined E and B maps, by making desired alterations to the radial filter. We demonstrate that these altered E mode and B mode constructions do not significantly distort spectral information on small angular scales.

Contents

1	Introduction	3
2	E/B description of CMB polarization	4
2.1	Polarization primer	4
2.2	Matrix notation	5
3	Real space operators	6
3.1	Evaluating E & B fields from measured Stokes parameters Q & U	7
3.2	Evaluating Stokes parameters Q & U fields from E & B fields	9
3.3	Decomposing Q & U Stokes parameters into those corresponding to E & B modes respectively	10
3.4	Visualizing the convolution kernels	13
3.5	Quantifying the non-locality of E & B modes	15
4	Numerical implementation	18
4.1	Constructing E & B maps using local convolutions	18
4.2	Separating Stokes Q & U maps corresponding to E & B modes of polarization	21
4.3	Multipole filtering using spatial convolutions	23
4.4	Application to Planck 353 Ghz polarization maps	26
4.5	Scaling and future prospects	26
5	Discussion	28
6	Appendix	30
6.1	Mathematical properties of spin spherical harmonics	30
6.2	Asymptotic forms for the functions $\pm_2 f_\ell(\beta)$	30
6.3	Convolution error	31
6.4	Local convolution kernels using standing Healpix routines	32
6.5	The correlation function and radial cut offs.	32
6.6	Explaining the oscillations in spectra and recovering the true spectra	33

Some comments, questions and ideas that occurred to me while writing the draft:

1. Using these local convolution can one now understand the E to B leakage occurring due to masking ?
2. Healpix has rings at constant latitude. So the real space convolution is only perfect for pixels near the pole ? What happens when you consider pixels around any arbitrary pixel on a Healpix map, they are probably not arranged in rings. Maybe for this reason working with upgraded map works and finer pixels allow for a better approximation of rings around arbitrary pixels ??
3. The Zaldariagga radial function $1/\theta^2$ cannot be correct, since it does not vanish at $\beta = \pi$, while it is defined to be zero at $\beta = 0$. I guess since its in the flat sky limit, the $\beta = \pi$ issue is not relevant.

To do list:

1. Check whether the local Healpix works for primordial B-mode spectrum.
2. Check the generation of local kernels by using a an effective beam in harmonic space. pl2 transformed
3. How do the coefficients of expansion for some radially compact kernel, derived from pl2 transforms differ from that of a pl0 transform ?

1 Introduction

In this work we follow the convention in which bar-ed variables correspond to those in real space, while the tilde-ed variables correspond to those in harmonic space [1].

This paper is organized in the following manner: In Sec. 2 we present a primer on the description of CMB polarization on the sphere and introduce the matrix notation which provides a more concise description of the same. In Sec. 3 we introduce the necessary tools and discuss the derivations of the real space operators. In Sec. 3.4 we evaluate the real space operators and present visualizations of these functions. Here we also discuss the locality of the real space E & B operators. In Sec. 4 we implement these operators to evaluate E & B maps from the Stokes parameters Q & U and compare these maps and their spectra from those derived using Healpix. We conclude with a discussion and the scope of this new method of analyzing CMB polarization in Sec. 5.

2 E/B description of CMB polarization

2.1 Polarization primer

The CMB polarization is measured in terms of Stokes Q and U parameters. These measurements can be combined to form the complex spin 2 polarization field as follows,

$$\begin{aligned}\pm_2 \bar{X}(\hat{n}) &= Q(\hat{n}) \pm iU(\hat{n}) \\ &= \sum_{\ell m} \pm_2 \tilde{X}_{\ell m} Y_{\ell m}(\hat{n}).\end{aligned}\quad (2.1)$$

Since these measured quantities depend on the local coordinate system, it is cumbersome to work with them. To overcome this, one describes the CMB polarization field in terms of a scalar field denoted by $E(\hat{n})$ and a pseudo scalar field $B(\hat{n})$ [2]. These scalar fields are related to the spin-2 polarization field $\pm_2 X(\hat{n})$ via the following relations,

$$\mathcal{E}(\hat{n}) = -\frac{1}{2} [\bar{\partial}_{+2}^2 X(\hat{n}) + \partial_{-2}^2 X(\hat{n})] ; \mathcal{B}(\hat{n}) = -\frac{1}{2i} [\bar{\partial}_{+2}^2 X(\hat{n}) - \partial_{-2}^2 X(\hat{n})], \quad (2.2)$$

where $\bar{\partial}$ and ∂ denote the spin raising and lowering operators respectively. These E and B fields are spin-0 fields similar to the temperature anisotropies and hence their value are independent of the coordinate system definitions (except that the B-modes have an odd parity, meaning that they change sign under reflection $\hat{n} \rightarrow -\hat{n}$). The spin raising and lowering operators have the following properties [3],

$$\bar{\partial}_s Y_{\ell m}(\hat{n}) = \sqrt{(\ell - s)(\ell + s + 1)} {}_{s+1} Y_{\ell m}(\hat{n}), \quad (2.3a)$$

$$\bar{\partial}_s Y_{\ell m}(\hat{n}) = -\sqrt{(\ell + s)(\ell - s + 1)} {}_{s-1} Y_{\ell m}(\hat{n}), \quad (2.3b)$$

where ${}_s Y_{\ell m}(\hat{n})$ denote the spin-s spherical harmonics.

Using Eq. (2.2) and the properties of the spin raising and lowering operators given in Eq. (2.3a) it can be shown that the scalar fields \mathcal{E}/\mathcal{B} are defined via the following set of equations,

$$\mathcal{E}(\hat{n}) = \sum_{\ell m} a_{\ell m}^E \sqrt{\frac{(\ell + 2)!}{(\ell - 2)!}} Y_{\ell m}(\hat{n}) ; \mathcal{B}(\hat{n}) = \sum_{\ell m} a_{\ell m}^B \sqrt{\frac{(\ell + 2)!}{(\ell - 2)!}} Y_{\ell m}(\hat{n}), \quad (2.4)$$

where the harmonic coefficients of \mathcal{E}/\mathcal{B} fields are related to the harmonic coefficients of the spin-2 polarization field via the following equations,

$$a_{\ell m}^E = -\frac{1}{2} [{}_{+2} X_{\ell m} + {}_{-2} X_{\ell m}] ; a_{\ell m}^B = -\frac{1}{2i} [{}_{+2} X_{\ell m} - {}_{-2} X_{\ell m}] \quad (2.5)$$

In the remainder of this article, we will work with the scalar E and pseudo scalar B fields as defined by the following expressions,

$$E(\hat{n}) = \sum_{\ell m} a_{\ell m}^E Y_{\ell m}(\hat{n}) ; B(\hat{n}) = \sum_{\ell m} a_{\ell m}^B Y_{\ell m}(\hat{n}). \quad (2.6)$$

Note that the $[E, B]$ fields are merely filtered versions of the fields $[\mathcal{E}, \mathcal{B}]$, as their spherical harmonic coefficients of expansion differ by the factor of $\sqrt{\frac{(\ell + 2)!}{(\ell - 2)!}}$. We make this choice since the CMB spectra are more closely related to the fields E & B.

2.2 Matrix notation

In this section we cast the relation introduced in Sec. 2.1 in matrix notation¹. This representation will make transparent the derivation of the real space operators we discuss in the following sections. We adopt a convention in which real space quantities are denoted by bar-ed variable while those in harmonic space are denoted by tilde-ed variables.

We begin by introducing the matrices encoding the spin spherical harmonic basis vectors,

$${}_{|s|}\mathcal{Y} = \begin{bmatrix} {}^{+s}Y & 0 \\ 0 & {}^{-s}Y \end{bmatrix}_{2N_{\text{pix}} \times 2N_{\text{alms}}}, \quad (2.7)$$

where s denotes the spin of the basis functions. For this work we will only be working with cases $s \in [0, 2]$. In this notation, each column can be mapped to a specific harmonic basis function marked by the pair of indices: (ℓ, m) and each row maps to a specific position on the sphere. Note that this matrix is in general not a square matrix. The number of rows is determined by the scheme used to discretely represent the sphere and the number of columns is set by the number of basis functions of interest (often determined by the band limit).

We now define the different polarization data vectors and their representation in real and harmonic space as follows,

$$\bar{S} = \begin{bmatrix} E \\ B \end{bmatrix}_{2N_{\text{pix}} \times 1} ; \quad \bar{X} = \begin{bmatrix} {}^{+2}X \\ {}^{-2}X \end{bmatrix}_{2N_{\text{pix}} \times 1} ; \quad \bar{P} = \begin{bmatrix} Q \\ U \end{bmatrix}_{2N_{\text{pix}} \times 1}, \quad (2.8a)$$

$$\tilde{S} = \begin{bmatrix} a^E \\ a^B \end{bmatrix}_{2N_{\text{alms}} \times 1} ; \quad \tilde{X} = \begin{bmatrix} {}^{+2}\tilde{X} \\ {}^{-2}\tilde{X} \end{bmatrix}_{2N_{\text{alms}} \times 1}. \quad (2.8b)$$

The different symbols have the same meaning as that discussed in Sec. 2.1, except that the subscript ℓ_m for the spherical harmonic coefficients of expansion is suppressed if favor of cleaner notation.

Next we define the operators which govern the transformations between different representations of the polarization field as follows,

$$\bar{T} = \begin{bmatrix} 1 & i\mathbb{1} \\ \mathbb{1} & -i\mathbb{1} \end{bmatrix}_{2N_{\text{pix}} \times 2N_{\text{pix}}} ; \quad \bar{T}^{-1} = \frac{1}{2}\bar{T}^\dagger, \quad (2.9a)$$

$$\tilde{T} = -\begin{bmatrix} 1 & i\mathbb{1} \\ \mathbb{1} & -i\mathbb{1} \end{bmatrix}_{2N_{\text{alms}} \times 2N_{\text{alms}}} ; \quad \tilde{T}^{-1} = \frac{1}{2}\tilde{T}^\dagger, \quad (2.9b)$$

where we have chosen the sign conventions so as to match those used in Healpix. Using the data vectors and the matrix operators defined above we can now express, in compact notation, the forward and inverse relations between different representations of the polarization data vectors as follows,

$$\bar{X} = \bar{T} * \bar{P} ; \quad \bar{P} = \frac{1}{2}\bar{T}^\dagger * \bar{X}, \quad (2.10a)$$

$$\bar{X} = {}_2\mathcal{Y} * \tilde{X} ; \quad \tilde{X} = {}_2\mathcal{Y}^\dagger * \bar{X}, \quad (2.10b)$$

$$\tilde{X} = \tilde{T} * \tilde{S} ; \quad \tilde{S} = \frac{1}{2}\tilde{T}^\dagger * \tilde{X}. \quad (2.10c)$$

$$\bar{S} = {}_0\mathcal{Y} * \tilde{S} ; \quad \tilde{S} = {}_0\mathcal{Y}^\dagger * \bar{S}. \quad (2.10d)$$

¹While we work with the matrix and vector sizes given in terms of some pixelization parameter N_{pix} , all the relations are equally valid in the continuum limit attained by allowing $N_{\text{pix}} \rightarrow \infty$

Next we introduce the harmonic space operators, which project the harmonic space data vector to E or B subspace,

$$\tilde{O}_E = \begin{bmatrix} 1 & 0 \\ 0 & 0 \end{bmatrix}_{2N_{\text{alms}} \times 2N_{\text{alms}}} ; \quad \tilde{S}_E = \tilde{O}_E * \tilde{S}, \quad (2.11a)$$

$$\tilde{O}_B = \begin{bmatrix} 0 & 0 \\ 0 & 1 \end{bmatrix}_{2N_{\text{alms}} \times 2N_{\text{alms}}} ; \quad \tilde{S}_B = \tilde{O}_B * \tilde{S} \quad (2.11b)$$

Note that these harmonic space matrices are idempotent, orthogonal to each other and their sum is an identity matrix as can be explicitly seen via the following relations,

$$\tilde{O}_E * \tilde{O}_E = \tilde{O}_E ; \quad \tilde{O}_B * \tilde{O}_B = \tilde{O}_B, \quad (2.12a)$$

$$\tilde{O}_E * \tilde{O}_B = \emptyset, \quad (2.12b)$$

$$\tilde{O}_E + \tilde{O}_B = \mathbb{1}. \quad (2.12c)$$

Note that the above relations for these harmonic space operators are exactly valid. In the following sections we aim to derive the real space analogues of these harmonic space operators.

3 Real space operators

In this section we derive the real space operators which translate the Stokes vector \bar{P} to the vector of scalars \bar{S} and vice versa. We also derive real space operators for direct decomposition of the Stokes vector \bar{P} in to a vector \bar{P}_E that correspond to E-modes and another vector \bar{P}_B that corresponds to the B-modes of polarization, such that $\bar{P} = \bar{P}_E + \bar{P}_B$ (without ever evaluating the E & B fields or their spherical harmonics). For carrying out these derivations we extensively use the matrix notation introduced in Sec. 2.2.

Euler angles: All the real space operators we derive are most conveniently expressed as functions of the Euler angles α , β & γ on the sphere. Owing to this fact we begin by briefly describing the Euler angles and present a way to think about them. The local cartesian coordinate system at any point on the sphere is defined such that the z-axis points along the radial direction, the x-axis is along the vector tangent to the local longitude pointing south and the y-axis is a vector tangent to the local latitude pointing east. The Euler angles define rotations that transforms the local cartesian coordinate system defined at the location $\hat{n}_0 \equiv (\theta_0, \phi_0)$ such that it aligns with the local cartesian coordinate system at the location $\hat{n}_i \equiv (\theta_i, \phi_i)$ [4]. The Euler angles can be evaluated using the following functions of the angular coordinates of the two locations $\hat{n}_0 \equiv (\theta_0, \phi_0)$ and $\hat{n}_i \equiv (\theta_i, \phi_i)$,

$$\tan \alpha = \frac{\sin(\phi_i - \phi_0) \sin \theta_i}{\sin \theta_i \cos \theta_0 \cos(\phi_i - \phi_0) - \sin \theta_0 \cos \theta_i}, \quad (3.1a)$$

$$\cos \beta = \sin \theta_i \sin \theta_0 \cos(\phi_i - \phi_0) + \cos \theta_i \cos \theta_0, \quad (3.1b)$$

$$\tan \gamma = \frac{-\sin(\phi_i - \phi_0) \sin \theta_0}{\sin \theta_0 \cos \theta_i \cos(\phi_i - \phi_0) - \sin \theta_i \cos \theta_0}, \quad (3.1c)$$

where α defines the rotation about the z-axis, β defines the rotation about the new y-axis (y1-axis) after the previous rotation and γ defines the rotation about the final z-axis (z2-axis) after carrying out the previous two rotations. In more physical terms, these angles can be understood as follow: The rotation by α about the z-axis is such that it aligns the x-axis of the cartesian system at location \hat{n}_0 along the great circle in the direction of \hat{n}_i . The rotation by

β about the y2-axis parallel transports the local cartesian coordinate system from location \hat{n}_0 to location \hat{n}_i , such that the z-axes of the two coordinate systems are parallel to each other. Finally the rotation by angle γ about the z2-axis aligns the x & y axes of the parallel transported system with those of the local cartesian system defined at \hat{n}_i . The simplest case is when one of the coordinates coincides with the north pole (more formally this refers to the point $\theta_0 \rightarrow 0$ while moving along the longitude $\phi_0 = 0$), say $\hat{n}_0 = (\theta_0, \phi_0) = (0, 0)$. In this case it is easy to check by substituting these coordinate values in Eq. (3.1a) that the Euler angles are: $(\alpha, \beta, \gamma) = (\phi_i, \theta_i, 0)$. While evaluating the above functions we follow the convention that β lies in the domain $[0, \pi]$ and that the angles α & γ lie in the domain $[-\pi, \pi]$. It is important to assign the proper signs to α & γ by duly accounting for the signs of the term in the numerator and the denominator. **While in following section we present results in terms of these Euler angles, the local kernels surrounding any pixel can be simply evaluated using standard Healpix functions. We give the details of this procedure in Appendix 6.4.**

3.1 Evaluating E & B fields from measured Stokes parameters Q & U

In Sec. 2.1 we described how the scalar fields E & B are derived from the Stokes parameters Q & U. To reiterate, this process involved taking the spin harmonic transform of the complex spin-2 field ($\pm_2 \tilde{X}$), taking linear combinations of the resultant coefficients of expansion ($\pm_2 \tilde{X}_{\ell m}$) and evaluating the forward spin-0 transform to derive the scalar E & B fields. Here we derive the real space convolution kernels on the sphere which can be used to directly evaluate the scalar E & B fields on the sphere. We use the relations given in Eq. (2.10), to write down an equation relating the real space vector of scalars \bar{S} to the polarization vector \bar{P} as given below,

$$\bar{S} = {}_0 \mathcal{Y} * \tilde{T}^{-1} * {}_2 \mathcal{Y}^\dagger * \bar{T} * \bar{P} = \frac{1}{2} {}_0 \mathcal{Y} * \tilde{T}^\dagger * {}_2 \mathcal{Y}^\dagger * \bar{T} * \bar{P}, \quad (3.2a)$$

$$= \bar{O} * \bar{P}. \quad (3.2b)$$

The explicit form of the real space operator \bar{O} can be derived by contracting over all the matrix operators. This procedure of contracting over the operators is explicitly worked out in the following set of equations,

$$\bar{O} = \frac{1}{2} {}_0 \mathcal{Y} * \tilde{T}^\dagger * {}_2 \mathcal{Y}^\dagger * \bar{T}, \quad (3.3a)$$

$$= -0.5 \begin{bmatrix} {}_0 Y_i & 0 \\ 0 & {}_0 Y_i \end{bmatrix} \begin{bmatrix} \mathbb{1} & \mathbb{1} \\ -i\mathbb{1} & i\mathbb{1} \end{bmatrix} \begin{bmatrix} {}^{+2} Y_j^{T*} & 0 \\ 0 & {}^{-2} Y_j^{T*} \end{bmatrix} \begin{bmatrix} \mathbb{1} & i\mathbb{1} \\ \mathbb{1} & -i\mathbb{1} \end{bmatrix}, \quad (3.3b)$$

$$= -0.5 \begin{bmatrix} \sum({}_0 Y_i {}_2 Y_j^{T*} + {}_0 Y_i {}_{-2} Y_j^{T*}) & i \sum({}_0 Y_i {}_2 Y_j^{T*} - {}_0 Y_i {}_{-2} Y_j^{T*}) \\ -i \sum({}_0 Y_i {}_2 Y_j^{T*} - {}_0 Y_i {}_{-2} Y_j^{T*}) & \sum({}_0 Y_i {}_2 Y_j^{T*} + {}_0 Y_i {}_{-2} Y_j^{T*}) \end{bmatrix}, \quad (3.3c)$$

where the symbol ${}_0 Y_i$ is used to denote the sub-matrix ${}_0 Y_{\hat{n}_i \times \ell m} \equiv {}_0 Y_{\ell m}(\hat{n}_i)$, the symbol ${}_{\pm 2} Y_j^{T*}$ is used to denote the matrix ${}_{\pm 2} Y_{\ell m \times \hat{n}_j}^* \equiv {}_{\pm 2} Y_{\ell m}^*(\hat{n}_j)$ and the summation is over the multipole indices ℓ, m . Using the conjugation properties of the spin spherical harmonic functions it can be shown that the following relation holds true,

$$\left[\sum_{\ell m} {}_0 Y_{\ell m}(\hat{n}_i) {}_{+2} Y_{\ell m}^*(\hat{n}_j) \right]^* = \sum_{\ell m} {}_0 Y_{\ell m}(\hat{n}_i) {}_{-2} Y_{\ell m}^*(\hat{n}_j). \quad (3.4)$$

where the terms on either side of the equation are those that appear in Eq. (3.3c). Therefore the different parts of the real space operator \bar{O} are completely specified in terms of the

complex function,

$$\begin{aligned} \mathcal{M}(\hat{n}_i, \hat{n}_j) &= \mathcal{M}_r + i\mathcal{M}_i, \\ &= \sum_{\ell m} {}_0Y_{\ell m}^*(\hat{n}_i) {}_2Y_{\ell m}(\hat{n}_j) = \sum_{\ell} \sqrt{\frac{2\ell+1}{4\pi}} {}_0Y_{\ell 2}(\beta_{ij}, \alpha_{ij}), \end{aligned} \quad (3.5a)$$

$$= \left[\cos(2\alpha_{ij}) + i \sin(2\alpha_{ij}) \right] \sum_{\ell=\ell_{\min}}^{\ell_{\max}} \frac{2\ell+1}{4\pi} \sqrt{\frac{(\ell-2)!}{(\ell+2)!}} P_{\ell 2}(\cos \beta_{ij}), \quad (3.5b)$$

$$= \left[\cos(2\alpha_{ij}) + i \sin(2\alpha_{ij}) \right] f(\beta_{ij}, \ell_{\min}, \ell_{\max}), \quad (3.5c)$$

where we have used the property of summation over spin spherical harmonics (see Eq. (6.1)) listed in Appendix 6.1. On simplifying Eq. (3.3c), the local convolution kernel can be cast in this simple form,

$$\bar{O} = - \begin{bmatrix} \mathcal{M}_r & \mathcal{M}_i \\ -\mathcal{M}_i & \mathcal{M}_r \end{bmatrix}_{2N_{\text{pix}} \times 2N_{\text{pix}}} = -f(\beta_{ij}, \ell_{\min}, \ell_{\max}) \begin{bmatrix} \cos(2\alpha_{ij}) & \sin(2\alpha_{ij}) \\ -\sin(2\alpha_{ij}) & \cos(2\alpha_{ij}) \end{bmatrix}, \quad (3.6)$$

where indices i,j map to the location \hat{n}_i and \hat{n}_j on the sphere. A similar equation for real space E & B operators was derived in [1], however those results were derived for the flat sky case and did not explicitly derive the radial kernel. \Rightarrow A discussion on this should be in the conclusions.

The scalar fields E & B can now be directly derived from the measured Stokes Q & U parameters by evaluating the following convolution,

$$\begin{bmatrix} E_i \\ B_i \end{bmatrix} = -\Delta\Omega \sum_{j=1}^{N_{\text{pix}}} f(\beta_{ij}, \ell_{\min}, \ell_{\max}) \begin{bmatrix} \cos(2\alpha_{ij}) & \sin(2\alpha_{ij}) \\ -\sin(2\alpha_{ij}) & \cos(2\alpha_{ij}) \end{bmatrix} \begin{bmatrix} Q_j \\ U_j \end{bmatrix}, \quad (3.7)$$

where $\Delta\Omega$ denotes the pixel area and all the symbols have their usual meaning. The above equation can be expressed more concisely as follows,

$$[E + iB](\hat{n}_0) = -\Delta\Omega \sum_{j=1}^{N_{\text{pix}}} \left(\sum_{\ell=\ell_{\min}}^{\ell_{\max}} \sqrt{\frac{2\ell+1}{4\pi}} P_{\ell}^2(\beta_{0j}) \right) \left(e^{-i2\alpha_{0j}} {}_2X(\hat{n}_j) \right), \quad (3.8a)$$

$$= - \left(\left[\sum_{\ell=\ell_{\min}}^{\ell_{\max}} \sqrt{\frac{2\ell+1}{4\pi}} Y_{\ell 2}^* \right] \circ {}_2X \right), \quad (3.8b)$$

where \circ denotes a convolution and the spherical harmonic functions denote the rotated functions such that the pole of the function coincides with the direction \hat{n}_0 and the reference zero for the azimuthal angle is the local longitude ϕ_0 . We know that the spin of product of functions with different spins is given by: $s_1 f s_2 g = s_{1+s_2} h$. Since $[Q + iU]$ is a field with spin +2 and the function $\exp(-i2\alpha)$ is a field with spin -2, the resultant field formed by the product of these two function has spin-0. This makes intuitive, the construction of the spin-0 E and B modes of polarization. Note that the coordinate dependence of the Stokes parameters cannot be integrated out at the location \hat{n}_0 where the scalar fields are to be evaluated since the azimuthal angle becomes ill-defined. This issue is averted by the fact that the radial function is formed by taking weighted linear combinations of P_{ℓ}^2 Legendre

polynomials which have vanishing contribution ($P_\ell^2(\beta) \propto \sin^2 \beta$) as $\beta \rightarrow 0, \pi$. Also note that the E-modes are constructed by product of functions ($U \sin 2\alpha, Q \cos 2\alpha$) which have the same parity and hence have even parity while the B-modes are constructed by multiplying functions ($Q \sin 2\alpha, U \cos 2\alpha$) of opposite parity and hence have an odd parity.

Note that this kernel does not depend on the Euler angle $\gamma \Rightarrow$ Why is that and how do you understand this? . This local convolution kernel has a part which depends only on the Euler angle α which has no multipole dependence. The remaining part of the kernel is specified by the function $f(\beta, \ell_{\min}, \ell_{\max})$ which depends only on the Euler angle β and completely incorporates the multipole ℓ dependence of the kernel. We will refer to $f(\beta, \ell_{\min}, \ell_{\max})$ as the radial part of the kernel since it only depends on the angular distance between different locations. Its the radial part of the kernel that completely determines the locality of this operator.

The azimuthal operations do not depend on the choice of basis functions, and can be argued as a requirement for constructing spin-0 fields by operating on spin-2 fields. The radial kernel however is determined by the choice of the basis functions. Motivated by this observation, one can now think of working with alternate basis functions which have different radial fall off. \Rightarrow This is generally true for all the local kernels. So shift this line to the section where we explore different radial functions.

3.2 Evaluating Stokes parameters Q & U fields from E & B fields

The real space operator which translates E & B fields to Stokes parameters Q & U is derived using a similar procedure. The inverse operator is given by the following expression,

$$\bar{P} = \bar{T}^{-1} * {}_2\mathcal{Y} * \tilde{T} * {}_0\mathcal{Y}^\dagger \bar{S} = \frac{1}{2} \bar{T}^\dagger * {}_2\mathcal{Y} * \tilde{T} * {}_0\mathcal{Y}^\dagger \bar{S} \quad (3.9)$$

$$= \bar{O}^{-1} * \bar{S} \quad (3.10)$$

We do not provide the explicit calculations here, since the derivation is nearly identical to that discussed in the previous section. The inverse operator is given by the following expression,

$$\bar{O}^{-1} = - \begin{bmatrix} \mathcal{M}_r & -\mathcal{M}_i \\ \mathcal{M}_i & \mathcal{M}_r \end{bmatrix}_{2N_{\text{pix}} \times 2N_{\text{pix}}} = -f(\beta_{ij}, \ell_{\min}, \ell_{\max}) \begin{bmatrix} \cos(2\alpha_{ij}) & -\sin(2\alpha_{ij}) \\ \sin(2\alpha_{ij}) & \cos(2\alpha_{ij}) \end{bmatrix}. \quad (3.11)$$

Note that the kernel is different by a mere change in sign on the off-diagonals of the block matrix as compared to Eq. (3.6). We can evaluate the Stokes Q & U parameters from the scalar E & B fields by evaluating the following expression,

$$\begin{bmatrix} Q_i \\ U_i \end{bmatrix} = -\Delta\Omega \sum_{j=1}^{N_{\text{pix}}} f(\beta_{ij}, \ell_{\min}, \ell_{\max}) \begin{bmatrix} \cos(2\alpha_{ij}) & -\sin(2\alpha_{ij}) \\ \sin(2\alpha_{ij}) & \cos(2\alpha_{ij}) \end{bmatrix} \begin{bmatrix} E_j \\ B_j \end{bmatrix}, \quad (3.12)$$

where all the symbols have their usual meaning. The above equation can again be expressed more concisely as follows,

$$[Q + iU](\hat{n}_0) = -\Delta\Omega \sum_{j=1}^{N_{\text{pix}}} \left(\sum_{\ell=\ell_{\min}}^{\ell_{\max}} \sqrt{\frac{2\ell+1}{4\pi}} P_\ell^2(\beta_{0j}) \right) \left(\mathbf{e}^{i\mathbf{2}\alpha_{0j}} [\mathbf{E} + i\mathbf{B}](\hat{\mathbf{n}}_j) \right), \quad (3.13a)$$

$${}_2X(\hat{n}_0) = - \left(\left[\sum_{\ell=\ell_{\min}}^{\ell_{\max}} \sqrt{\frac{2\ell+1}{4\pi}} Y_{\ell 2} \right] \circ [E + iB] \right), \quad (3.13b)$$

which is to be interpreted in the same manner as Eq. (3.8). Note that the only change in the convolution kernel as compared to that in Eq. (3.6) is that the signs of the off-diagonal block matrices are reversed. Alternatively, the $Y_{\ell 2}$ functions are not conjugated. This can again be simply understood as constructing a spin-2 field by taking a product of a spin-0 field: $[E + iB]$ with a spin +2 field: $\exp(+i2\alpha)$. The radial dependence of the operator \bar{O}^{-1} is identical to the that of \bar{O} as one may have expected. In this case all the coordinate dependence is encoded in the function $\exp(+i2\alpha)$, which is ill-defined at the poles ($\beta \rightarrow 0, \pi$) and hence the radial functions have to vanish at these locations, which is the case for the same reasons discussed previously.

⇒ How does the radial kernel reduce to unity on evaluating the the operator on to its inverse ? This will be important to understand how to define alternate radial functions.

3.3 Decomposing Q & U Stokes parameters into those corresponding to E & B modes respectively

The Stokes Q & U parameters can be decomposed into the scalar modes E & B and vice versa, as seen in the previous sections. The E & B modes are orthogonal to each other, in the sense that their respective operators are orthogonal to each other as seen in Eq. (2.12b). It is possible to decompose the Stokes vector \bar{P} into one \bar{P}_E that purely contributes to E modes and another \bar{P}_B that purely contribute to the B modes of polarization. We can only measure the total Stokes vector which is a sum of the Stokes vectors corresponding to the respective scalar modes. In this section we derive the real space operators which directly perform this decomposition, without ever having to evaluate the E & B modes. The derivation is similar to that discussed in Sec. 3.1, though the algebra is a little more involved in this case. Here we use the harmonic space projection operators $\tilde{O}_{E/B}$, defined in Eq. (2.11), to derive the respective real space operators. The Stokes parameters corresponding to each scalar mode are given by the following expressions,

$$\bar{P}_E = [\bar{T}^{-1} * {}_2\mathcal{Y} * \tilde{T} * \tilde{O}_E * \tilde{T}^{-1} * {}_2\mathcal{Y}^\dagger * \bar{T}] * \bar{P}, \quad (3.14)$$

$$\begin{aligned} &= [\frac{1}{4}\bar{T}^\dagger * {}_2\mathcal{Y} * \tilde{T} * \tilde{O}_E * \tilde{T}^\dagger * {}_2\mathcal{Y}^\dagger * \bar{T}] * \bar{P}, \\ &= \bar{O}_E * \bar{P}, \end{aligned}$$

$$\bar{P}_B = [\bar{T}^{-1} * {}_2\mathcal{Y} * \tilde{T} * \tilde{O}_B * \tilde{T}^{-1} * {}_2\mathcal{Y}^\dagger * \bar{T}] * \bar{P}, \quad (3.15)$$

$$\begin{aligned} &= [\frac{1}{4}\bar{T}^\dagger * {}_2\mathcal{Y} * \tilde{T} * \tilde{O}_B * \tilde{T}^\dagger * {}_2\mathcal{Y}^\dagger * \bar{T}] * \bar{P}, \\ &= \bar{O}_B * \bar{P}. \end{aligned}$$

We contract over all the matrix operators to arrive at the the real space operators. On working through the algebra it can be shown that the real space operators have the following form,

$$\bar{O}_{E/B} = 0.5 \begin{bmatrix} \mathcal{I}_r & \mathcal{I}_i \\ -\mathcal{I}_i & \mathcal{I}_r \end{bmatrix} \pm \begin{bmatrix} \mathcal{D}_r & \mathcal{D}_i \\ \mathcal{D}_i & -\mathcal{D}_r \end{bmatrix}, \quad (3.16)$$

where \mathcal{I}_r & \mathcal{D}_r and \mathcal{I}_i & \mathcal{D}_i are the real and complex parts of the following complex functions,

$$\begin{aligned} \mathcal{I} &= \mathcal{I}_r + i\mathcal{I}_i = \sum_{\ell m} {}_{-2}Y_{\ell m}(\hat{n}_i) {}_{-2}Y_{\ell m}^*(\hat{n}_j), \\ \mathcal{D} &= \mathcal{D}_r + i\mathcal{D}_i = \sum_{\ell m} {}_2Y_{\ell m}(\hat{n}_i) {}_{-2}Y_{\ell m}^*(\hat{n}_j). \end{aligned}$$

These functions can be further simplified using the properties of spin spherical harmonics listed in Appendix 6.1. Specifically it can be shown that these functions reduce to the following mathematical forms,

$$\mathcal{I}(\hat{n}_i, \hat{n}_j) = \sum_{\ell} \sqrt{\frac{2\ell+1}{4\pi}} {}_{-2}Y_{\ell 2}(\beta_{ij}, \alpha_{ij}) e^{i2\gamma_{ij}} = \mathcal{I}_r + i\mathcal{I}_i, \quad (3.17a)$$

$$\mathcal{I}_r + i\mathcal{I}_i = \left[\cos(2\alpha_{ij} + 2\gamma_{ij}) + i \sin(2\alpha_{ij} + 2\gamma_{ij}) \right] {}_{-2}f(\beta_{ij}, \ell_{\min}, \ell_{\max}), \quad (3.17b)$$

$$\mathcal{D}(\hat{n}_i, \hat{n}_j) = \sum_{\ell} \sqrt{\frac{2\ell+1}{4\pi}} {}_2Y_{\ell 2}(\beta_{ij}, \alpha_{ij}) e^{-i2\gamma_{ij}} = \mathcal{D}_r + i\mathcal{D}_i, \quad (3.18a)$$

$$\mathcal{D}_r + i\mathcal{D}_i = \left[\cos(2\alpha_{ij} - 2\gamma_{ij}) + i \sin(2\alpha_{ij} - 2\gamma_{ij}) \right] {}_{+2}f(\beta_{ij}, \ell_{\min}, \ell_{\max}), \quad (3.18b)$$

where the functions,

$${}_{\pm 2}f(\beta, \ell_{\min}, \ell_{\max}) = \sum_{\ell=\ell_{\min}}^{\ell_{\max}} \sqrt{\frac{2\ell+1}{4\pi}} {}_{\pm 2}f_{\ell}(\beta), \quad (3.19)$$

can be expressed in terms of P_{ℓ}^2 Legendre polynomials and are given by the following explicit mathematical forms,

$$\begin{aligned} {}_{\pm 2}f_{\ell}(\beta) &= 2 \frac{(\ell-2)!}{(\ell+2)!} \sqrt{\frac{2\ell+1}{4\pi}} \left[-P_{\ell}^2(\cos \beta) \left(\frac{\ell-4}{\sin^2 \beta} + \frac{1}{2}\ell(\ell-1) \pm \frac{2(\ell-1)\cos \beta}{\sin^2 \beta} \right) \right. \\ &\quad \left. + P_{\ell-1}^2(\cos \beta) \left((\ell+2) \frac{\cos \beta}{\sin^2 \beta} \pm \frac{2(\ell+2)}{\sin^2 \beta} \right) \right]. \end{aligned} \quad (3.20)$$

Finally, the Stokes parameters corresponding to the respective scalar fields are given by evaluating the following expressions,

$$\begin{aligned} \begin{bmatrix} Q_i \\ U_i \end{bmatrix}_{E/B} &= \sum_{j=1}^{N_{\text{pix}}} \left\{ {}_{-2}f(\beta_{ij}, \ell_{\min}, \ell_{\max}) \begin{bmatrix} \cos(2\alpha_{ij} + 2\gamma_{ij}) & \sin(2\alpha_{ij} + 2\gamma_{ij}) \\ -\sin(2\alpha_{ij} + 2\gamma_{ij}) & \cos(2\alpha_{ij} + 2\gamma_{ij}) \end{bmatrix} \begin{bmatrix} Q_j \\ U_j \end{bmatrix} \right. \\ &\quad \left. \pm {}_{+2}f(\beta_{ij}, \ell_{\min}, \ell_{\max}) \begin{bmatrix} \cos(2\alpha_{ij} - 2\gamma_{ij}) & \sin(2\alpha_{ij} - 2\gamma_{ij}) \\ \sin(2\alpha_{ij} - 2\gamma_{ij}) & -\cos(2\alpha_{ij} - 2\gamma_{ij}) \end{bmatrix} \begin{bmatrix} Q_j \\ U_j \end{bmatrix} \right\} 0.5\Delta\Omega, \end{aligned} \quad (3.21)$$

where all the symbols have their usual meaning. The above expression can be cast in the following simplified form,

$${}_{+2}X_{E/B} = 0.5\Delta\Omega \sum_{j=1}^{N_{\text{pix}}} {}_{-2}f(\beta_{ij}) e^{-i2(\alpha_{ij} + \gamma_{ij})} {}_{+2}X_j \pm {}_{+2}f(\beta_{ij}) e^{i2(\alpha_{ij} - \gamma_{ij})} {}_{+2}X_j^*, \quad (3.22a)$$

$$= 0.5 \left\{ I^* \circ {}_{+2}X \pm D \circ {}_{+2}X^* \right\}, \quad (3.22b)$$

where in Eq. (3.22a) we have suppressed the explicit multipole dependence of functions $\pm_2 f$ for brevity and in Eq. (3.22b) \circ denotes a convolution.

It is easy to show that the operator D is a complex but symmetric matrix and that the operator I is Hermitian. The function I is a band limited version of the delta function ($\lim_{\ell \rightarrow \infty} I = \delta(\hat{n}_i - \hat{n}_j)$), when interpreted as a matrix operator forms a band limited version of the identity matrix. Though its non-local ($I \neq 0$ when $\hat{n}_i \neq \hat{n}_j$) owing to the band limit, for all practical purposes the operator I acts like an identity operator as is confirmed by the following identities it satisfies: (i) $I * I = I$; (ii) $D * I = D$. Also D^* is the inverse of D in this band limited sense: $D^* * D = I$. Using these properties of the operators I and D , one can verify that the real space operators satisfy the following identities,

$$\bar{O}_E * \bar{O}_E = \bar{O}_E ; \quad \bar{O}_B * \bar{O}_B = \bar{O}_B , \quad (3.23a)$$

$$\bar{O}_E * \bar{O}_B = 0 , \quad (3.23b)$$

$$\bar{O}_E + \bar{O}_B = I , \quad (3.23c)$$

which are the real space analogues of Eq. (2.12). While testing the above stated identities one encounters terms like $D * I^*$, $I^* * I$ and $I * I^*$ which cannot be simply interpreted, but they always occur in pairs with opposite signs, hence exactly canceling each other. Note that unlike in the harmonic case, the sum of the operators is not exactly an identity matrix. \Rightarrow Isn't it possible to do some real space operations which doesn't care for the band limit but still returns the required decomposition into the respective scalar modes? This indicates the loss of information occurred from the original data due to making this transformations with some assumed band limit. If one forces the sum of the operators to be exactly an identity operator, then one compromises on the orthogonality property of the \bar{O}_E & \bar{O}_B operators.

3.4 Visualizing the convolution kernels

As seen in the previous sections, all the kernels separate into a part which depends only on the angular distance between pixels and another part that depends on the azimuthal orientation around the central pixel. The radial part of the kernels determines the non-locality of the operator. We numerically compute the radial kernels: $f_{,+2}f$ & $-_2f$ by evaluating the respective multipole sums given in Eq. (3.5b) and Eq. (3.19) in the band limit $\ell \in [= 2, 192]$. The resultant functions are depicted in Fig. 1. Note that the function $f(\beta)$, which forms

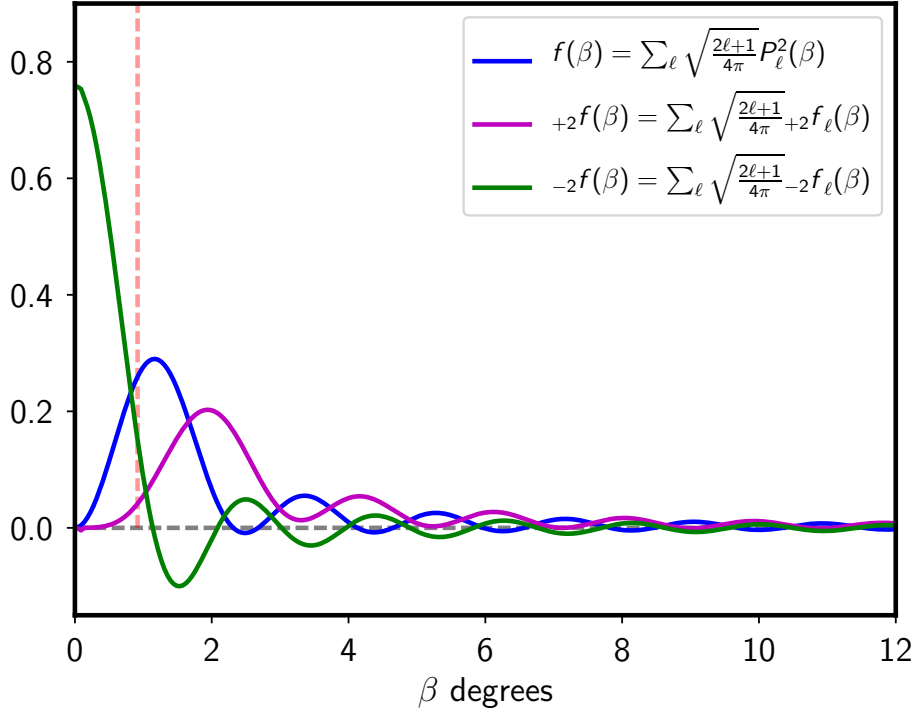


Figure 1. The figure depicts the radial part of the convolution kernels. These radial function have been evaluated with the band limit fixed at $\ell \in [2, 192]$. The vertical dashed line marks the approximate size of a NSIDE=64 Healpix pixel.

the radial part of the real space convolution kernel that translates the Stokes parameters Q & U to scalars E & B , has a vanishing contribution from the location of the central pixel ($\beta \rightarrow 0$). Recall that the fields E & B are scalar and hence expected to be immune to coordinate definitions. The locally defined Stokes parameters however necessarily depend on the coordinate definition. Therefore, this nature of the radial kernel is to be expected in order for it to satisfy the requirement of the derived quantities being coordinate independent.

The functions $+_2f(\beta)$ & $-_2f(\beta)$, both contribute to the convolution kernels which decompose the Stokes parameters into those corresponding to the respective scalar modes E & B . $-_2f(\beta)$ form the radial part of the band limited delta function I and hence it contributes the most at the location of the central pixel. $+_2f(\beta)$ again has a vanishing contribution near the central pixel and it dominantly contributes in the neighbouring regions which are approximately at least 1 pixel distance away from the central pixel.

The azimuthal dependencies of the convolution kernels, are specified as functions of the Euler angles α & γ . We evaluate the real and imaginary parts of the functions \mathcal{M} , \mathcal{D} & \mathcal{I} by

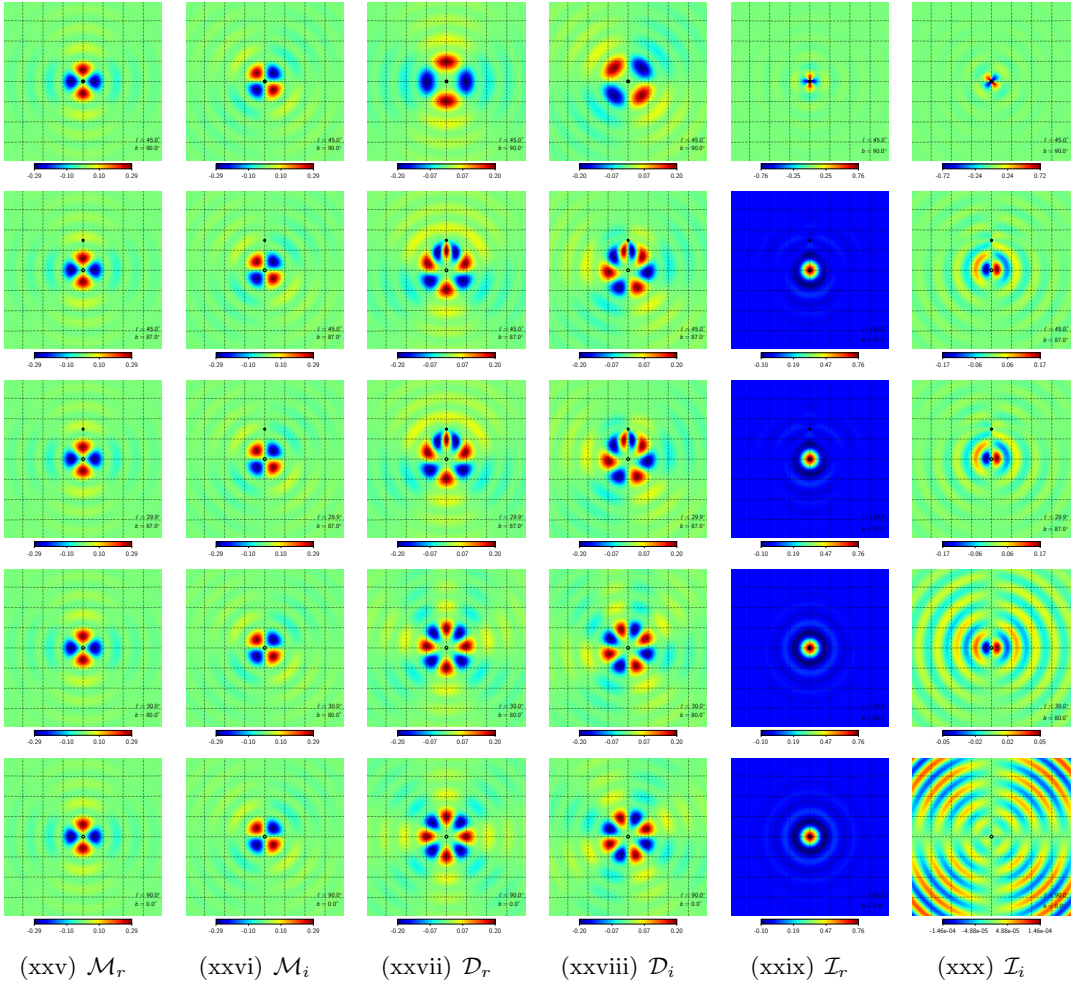


Figure 2. This panel of figure depicts the various parts of the convolution kernel, discussed in Sec. 3. These kernels have been evaluated with the band limit: $\ell \in [2, 192]$. The functions have been sampled at an NSIDE=2048 resolution for visual appeal. The size of each panel is approximately $16^\circ \times 16^\circ$ and the grid lines are marked at 2 degree separations. The black circles denotes the position of the central pixel around which the convolution kernels have been evaluated. The black star marks the location of the north galactic pole. The five rows depict the kernels at different location on the sphere and the galactic coordinates of the central pixel are specified in each panel.

calculating the Euler angles for all the pixels surrounding the central pixel and using them in Eq. (3.6), Eq. (3.17a) and Eq. (3.18a) respectively. Since its not easy to imagine how the Euler angles vary as a function of position of the central pixel, we evaluate and depict the kernels at different locations, to give a sense of how these kernels vary across the sphere. For illustration these functions are sampled at a very high Healpix resolution parameter of NSIDE=2048. All the plots have been rotated such that the pixel around which the kernels are evaluated lies in the centre marked by the back circle. The results are depicted in Fig. 2.

The function \mathcal{M} is identical irrespective of changes in the galactic latitude and longitude of the central pixel. The only contrasting locations are the poles (i.e. $|b| = 90^\circ$), where the functions \mathcal{M}_r & \mathcal{M}_i are rotated by 45° as compared to the respective functions evaluated at locations where $|b| \neq 90^\circ$. Also note that these functions are not distorted when a part

of the domain overlaps with the poles, as can be seen in the first three rows of Fig. 2. Both these facts can be associated with the fact that this function does not depend on the Euler angle γ . Recall that the angle γ defines the rotation about the final z-axis which co-aligns the planar axes. Since the function \mathcal{M} does not depend of this final orientation, it implies a rotational invariance of the fields constructed by convolving with this kernel.

The function \mathcal{D} varies significantly as a function of galactic latitude of the central pixel. It varies from having a two fold symmetry at the poles to having a four fold symmetry at the equator as seen in the middle two columns of Fig. 2. This change in behavior is primarily due to the dependence on the Euler angle γ . When the central pixel is nearly at the pole, γ vanishes, and the azimuthal part of the function D is identical to that of \mathcal{M} and hence the two function look very similar as seen in the first row of Fig. 2. Also note that this function is distorted as parts of its domain pass the galactic poles.

The function \mathcal{I} shows similar behavior, varying with latitude, having an identical azimuthal behavior near the poles and being distorted in parts that overlap with the galactic poles. This function, in the case of an infinite band limit reduces to a delta function at the position of the central pixel ($\lim_{\ell_{\max} \rightarrow \infty} : \mathcal{I}_r \rightarrow \delta(\hat{n}_0 - \hat{n}'), \mathcal{I}_i \rightarrow 0$), as discussed previously. Hints of this behavior can be seen by comparing the amplitudes of the real and imaginary parts of this function near the equator, depicted in the fifth row of the last two columns of Fig. 2. However note that this function significantly deviates from this behavior at higher galactic latitudes. The real and imaginary parts of this function contribute nearly equally near the vicinity of the poles. We invariably work with a specific band limit, hence both the real and imaginary parts of this functions make important non-zero contributions.

We reiterate that all the function are invariant under changes in longitude of the central pixel, the latitude being held fixed as can be seen by comparing the figures in the second row (evaluated at $[b, \ell] = [87^\circ, 45^\circ]$) and third row (evaluated at $[b, \ell] = [87^\circ, 30^\circ]$) of Fig. 2, as one may have expected.

3.5 Quantifying the non-locality of E & B modes

It is clear from previous discussions that that the non-locality of the E and B modes is determined by the radial part of the convolution kernels. To quantify this non-locality as a function of the maximum multipole accessible for analysis, we evaluate the radial part of the convolution kernel for different values of ℓ_{\max} , while keeping the lowest multipole fixed at $\ell_{\min} = 2$. The set of radial kernels so derived are plotted in Fig. 3. All the function have been normalized such that their global maxima is set to unity. Note that on increasing ℓ_{\max} the radial kernels shift to the left, attaining fractions of their global maxima at progressively small angular distances β from the central pixel.

We have observed that the radial functions derived by evaluating the multipole sums to different maximum multipoles are self similar. Specifically these functions follow an interesting telescoping and scaling property:

$${}_rf(\beta, 2, \ell_{\max}) \approx \left[\frac{\ell_{\max}}{\ell'_{\max}} \right]^2 {}_rf(\beta' = \frac{\ell_{\max}}{\ell'_{\max}} \beta, 2, \ell'_{\max}),$$

where ${}_rf$ denotes all the different radial functions. We can understand the shifting left of the radial kernels on increasing the maximum multipole using this property. Lets say the function ${}_rf(\beta, \ell'_{\max})$ transition to being monotonously below some fraction of the global maxima at an angular distance of β_0 . The function ${}_rf(\beta', \ell_{\max})$, given $\ell_{\max} > \ell'_{\max}$, reaches the same transition point $\beta' = \beta_0$ at a smaller value of β owing to the fact that ℓ_{\max}/ℓ'_{\max} is greater

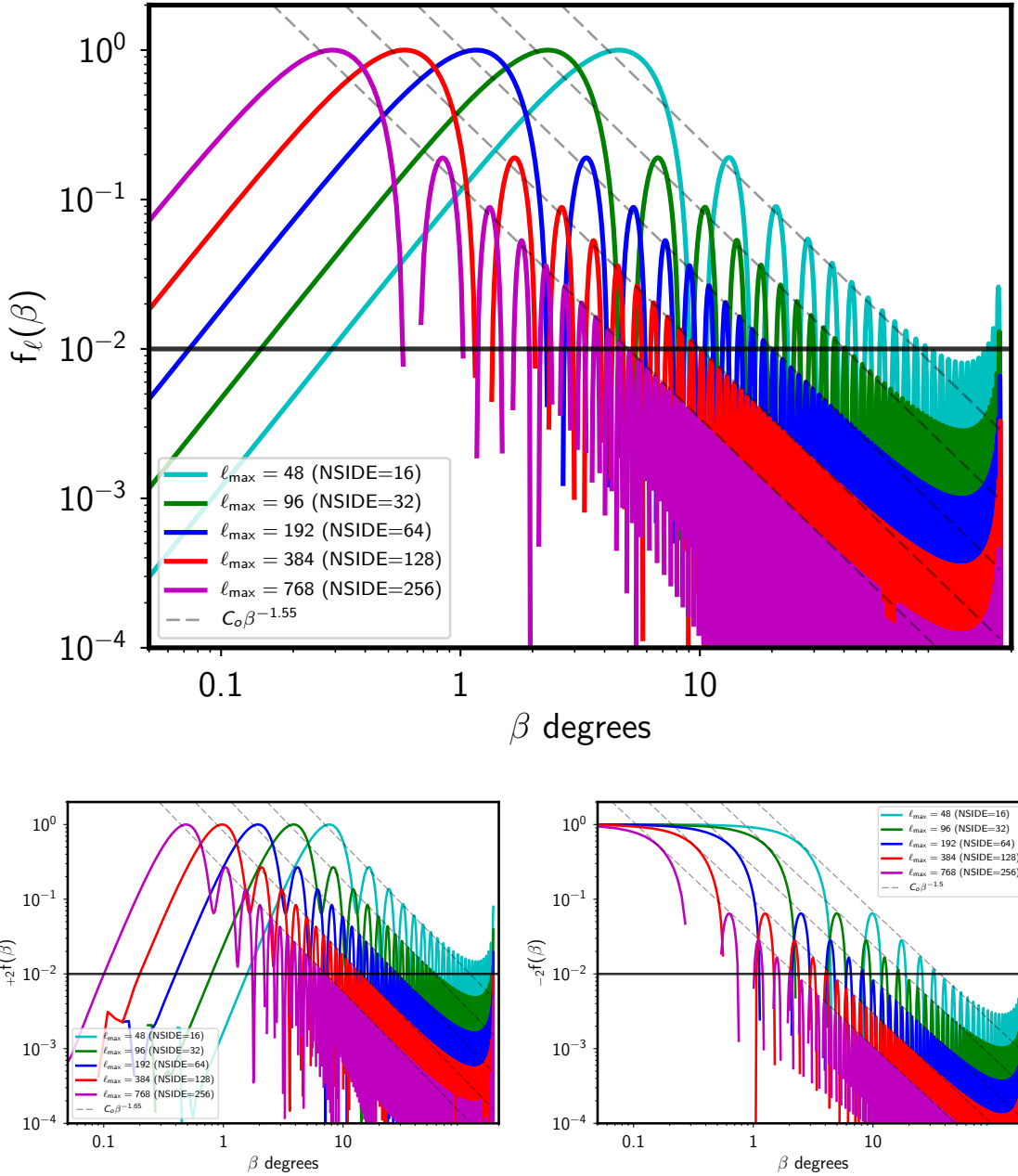


Figure 3. The top panel shows a plot of the radial kernels $f(\beta, \ell_{\min}, \ell_{\max})$ while the bottom left and right panels show the radial functions ${}_{+2}f(\beta, \ell_{\min}, \ell_{\max})$ & ${}_{-2}f(\beta, \ell_{\min}, \ell_{\max})$ respectively, for different ℓ_{\max} as indicated by the legends and fixed $\ell_{\min} = 2$. The curves for each of these functions have been normalized such that the maximum of the curve is set to unity. The horizontal solid black line marks the location where the amplitude of the kernel falls below 1% of its maximum. The slanted dashed black lines indicate a power law fit (by eye) to the envelope of the radial functions. While the envelopes for function $f(\beta)$ & ${}_{-2}f(\beta)$ are fit well by the power law $\propto \beta^{-1.5}$, the envelope for the function ${}_{+2}f(\beta)$ is seen to have a slightly steeper fall off $\propto \beta^{-1.65}$.

than unity. The amplitude scaling of the functions is irrelevant since the transition point is always described in terms of the fraction of the global maxima of the function.

We are primarily interested in the non-local dependence of the scalar modes E & B on the Stokes parameters Q & U. We define the value of the abscissa at which the function $f(\beta, \ell_{\min}, \ell_{\max})$ transits to being monotonously below 1% of the maxima of the function as the non-locality parameter: β_o . For a $\ell_{\max} = 24$, the maximum multipole accessible on a Nside=8 Healpix map, the non-locality parameter $\beta_0 = 180^\circ$, since the radial function never falls monotonously below 1% of the global maxima of the function. Using the self similar property of the radial function discussed above, we define the following: $\beta_o = \min(180, 180 \frac{24}{\ell_{\max}})$ as the non-locality parameter, given the maximum multipole ℓ_{\max} . β_0 is not very sensitive to ℓ_{\min} , though it can be important on making drastic changes to ℓ_{\min} . \Rightarrow Quantify how changing ℓ_{\min} changes β_0

The envelope of the radial kernel $f(\beta, \ell_{\min}, \ell_{\max})$ is observed to have a power law relation to the angular distance β as seen in Fig. 3. At small values of β , which corresponds to the flat sky limit, the radial function is proportional to β^2 . In the intermediate range, a fit by eye indicates that the envelope of the function is well represented by the power law $\beta^{-1.5}$. \Rightarrow There isn't too much of a discussion surrounding the function $\pm f(\beta)$.

4 Numerical implementation

As discussed in Sec. 3.5, the radial kernels decay ($\propto \beta^{-1.5}$) as the distance from the central pixel increases, but they begin to increase on approaching the diametrically opposite position ($\beta \rightarrow \pi$) as seen in Fig. 3. For a map containing sufficiently high multipole ℓ_{\max} information, the local maxima the radial kernel attains in the vicinity of the diametrically opposite end is significantly smaller than global maxima. This suggests that for sufficiently high resolution CMB maps, it may suffice to restrict the convolution over the Stoke parameters Q & U to a local region around the central pixel. The size of this local region is determined by the non-locality parameter β_o . **It is important to note that this claim is valid only while working with maps that are fairly homogeneous.** In the case of foregrounds for example, though the radial kernel falls off, a strong foreground very far from the central pixel may still make significant contribution to the local definition of E and B modes.

In this section we study the effects of localizing the convolution kernels on the inferred E and B mode maps and their power spectra. We have developed a Python script to compute these local convolution over Stokes Q & U parameters. To carry out this numerical exercise, we pre-compute the radial part of the kernels, namely the function: $f(\beta)$, $+_2f(\beta)$ & $-_2f(\beta)$. We use the python routine `scipy.special.lpmn` for the numerical evaluation of the associated Legendre polynomial functions required to compute the respective radial kernels following equations Eq. (3.5b) and Eq. (3.19). Specifically while computing the functions $+_2f(\beta)$ & $-_2f(\beta)$ in the vicinity of $\beta = 0$ & π , we use the limiting forms of the respective functions given in Appendix 6.2. As the next step, for each pixel on the Healpix map we get the pixel numbers of all the neighboring pixels lying within radius of r_{cutoff} from the central pixel using the Healpix routine `query_disc`. We then use the `pix2ang` function of Healpix to get the angular coordinates of the central (θ_o, ϕ_o) and its surrounding pixels (θ_i, ϕ_i) , which are used to calculate the corresponding Euler angles using Eq. (3.1a). Given these inputs we evaluate the convolutions as simple Reimann sums. We repeat this procedure for each pixel on the Healpix map to yielding the resultant maps (E, B, Q, U).

We use the CMB spectra for a fiducial cosmology and restrict our analysis on lensing induced B-mode spectra. For the results presented in the following sections we carry out our analysis on CMB maps at Healpix resolution of NSIDE = 64. In order to understand the effects of restricting the convolution to a local neighbourhood, we evaluate these convolutions on discs with progressively smaller radii surrounding the central pixel. Specifically the non-locality parameter for a NSIDE=64 map is $\beta_o = 22.5^\circ$. We impose radial cutoffs of $r_{\text{cutoff}} = [2\beta_o, \beta_o, 0.5\beta_o, 0.25\beta_o]$ with an apodization of 3 degrees having a cosine squared profiles on the edges of the discs. We also evaluate the corresponding maps using standard full sky Healpix routines and use these as reference maps for this exercise. Note that the Healpix evaluations are equivalent to carrying out the convolutions over the full sphere (i.e. $\beta_o = \pi$). We compare these maps to the reference maps and their respective spectra, to quantitatively understand the effect of the imposed radial cutoff on the convolutions.

4.1 Constructing E & B maps using local convolutions

Here we present the results of evaluating the local convolution given in Eq. (3.6), to derive E & B mode maps given maps of Stokes Q & U. The resultant maps are depicted in Fig. 4. Specifically the left column depicts the reference E & B maps derived using Healpix, the middle column depicts the E & B mode maps derived from local convolutions restricted to $2\beta_o$ and difference between these maps is depicted in the right column. The differences between

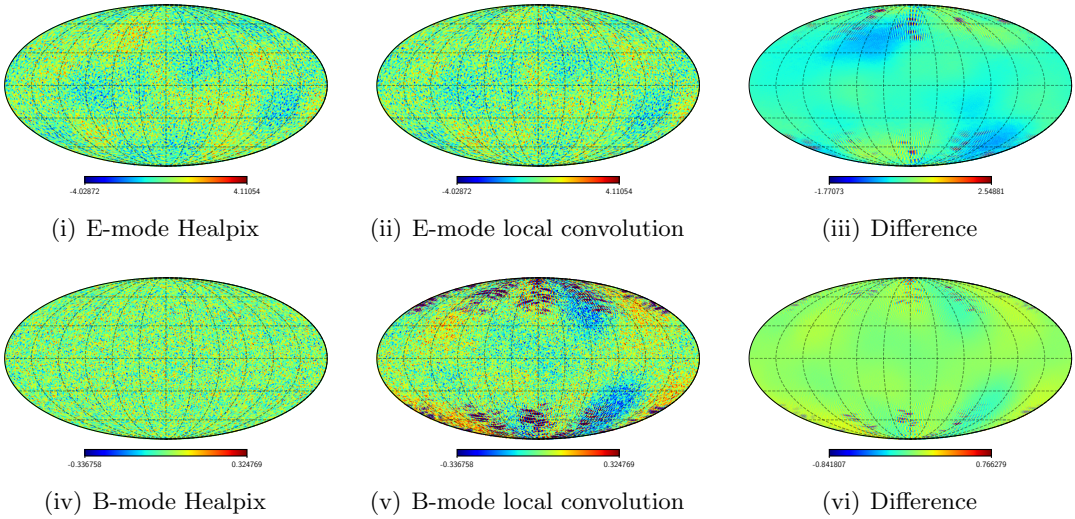


Figure 4. Left: Reference E & B mode maps derived using Healpix. Middle: E & B mode maps derived using $r_{\text{cutoff}} = 2\beta_o$. The color scale is saturated to that of the respective reference maps. Right: Difference between the maps shown in the left and middle columns.

these maps are observed to be large near the polar caps, however they are significantly smaller in the band around the equator. Further note that the differences seen around the equator are dominated by large scale modes, in contrast to the polar caps where one even observes small scale fluctuations.

Next we compute the power spectra of these local E & B maps and compare them to the spectra derived from the reference maps. The results of this exercise are summarized in Fig. 5. We note that when the radial cutoff is set much below the non-locality parameter as in $r_{\text{cutoff}} = 0.25\beta_o$, the spectra differ from the reference spectra by more than the cosmic variance. However on increasing the radial cutoff to only $0.5\beta_o$, the differences at most multipoles reduce to being comparable to the cosmic variance. On further increasing the radial cutoff to β_o and $2\beta_o$, the difference at most multipoles further reduce to levels of 0.5 cosmic variance or in absolute terms the differences are at the level of 2%. Also note that the improvement while transitioning from $r_{\text{cutoff}} = \beta_o$ to $r_{\text{cutoff}} = 2\beta_o$ are not as significant as seen while increasing the r_{cutoff} to β_o . This is can be understood as a consequence of the rapidly decaying nature of the radial kernels we discussed in Sec. 3.5.

At first glance, the above remarks seem to hold true only for the E mode spectra, since the errors in the B mode spectra seem to be significantly larger as seen in the middle row of Fig. 5. We understand that the higher error in the B mode spectra is primarily a combined effect of the low amplitude of the B mode spectrum as compared to the E mode spectrum and limited numerical accuracy of our simple convolution algorithm. We ran a number of tests to confirm these as reasons for the observed discrepant behaviour. We exchanged the E and B mode spectra, (taking care to set $C_\ell^{TE} = 0$) and noted that the trends observed in the error plots are reversed, clearly indicating a dependence on the amplitude of the spectrum. We noted that the polar caps were particularly error prone, as seen in Fig. 4. We excised these error prone regions, specifically masking portions of the maps with $|b| > 30^\circ$ to find that the errors on the B mode spectra revert to having very similar structure as that of the E mode spectra, as seen in the bottom row of Fig. 5. Finally we modify the use of standard

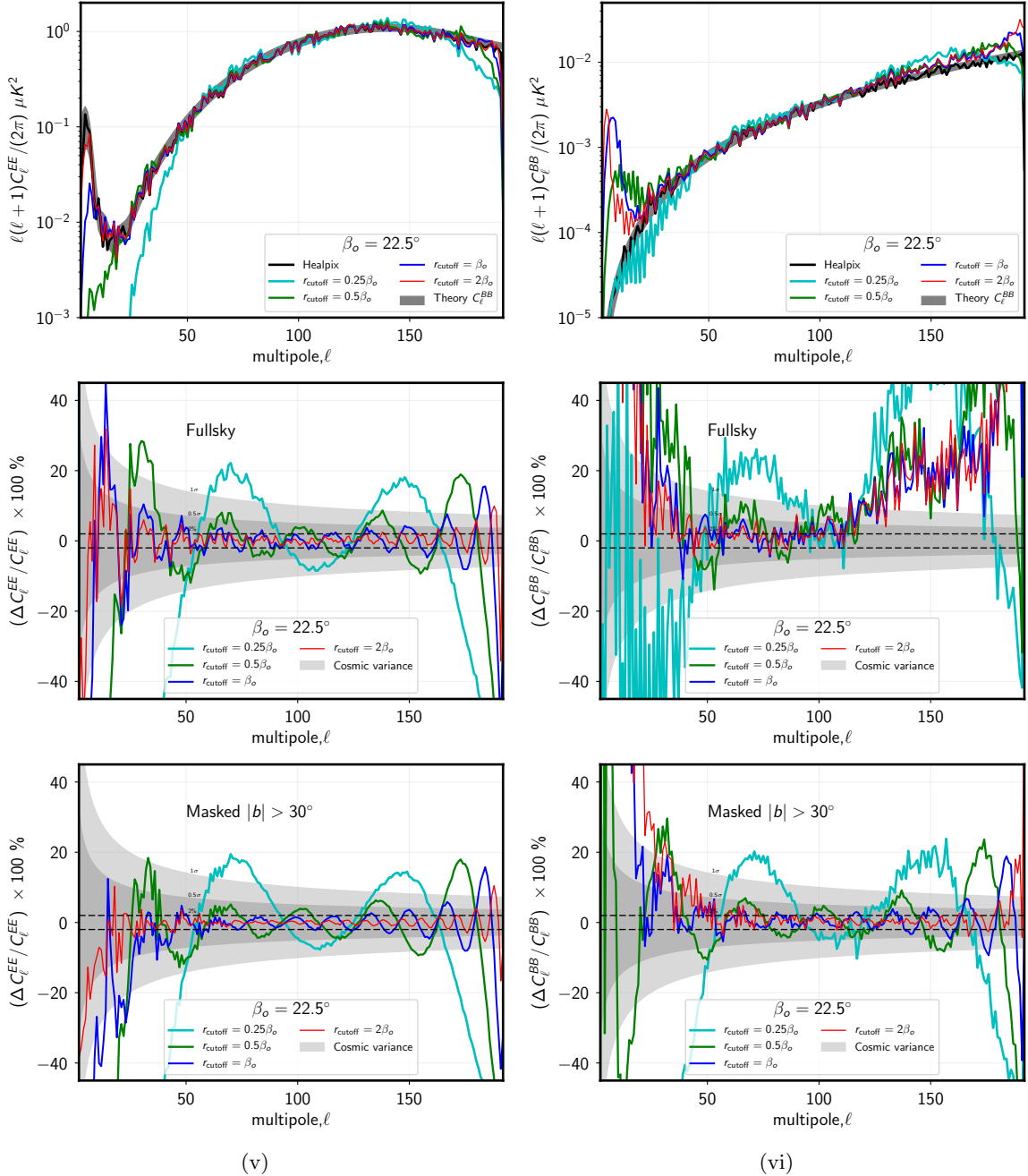


Figure 5. *Top:* The figures on left and right depict the E mode spectra and the B mode spectra respectively. *Middle:* These figures depict the relative percentage difference between the spectra derived from full sky, locally evaluated E & B maps and the reference spectra. *Bottom:* These figures depict the same results as shown in the middle row, except that the regions with $|b| > 30^\circ$ of the maps have been masked for this analysis. The colors indicate the spectra derived from imposing different radial cutoff as indicated by the legends. The gray bands indicate the cosmic variance scatter around the fiducial spectra. The dashed horizontal black lines mark the 2% error.

Healpix routines to mimic the local convolution E & B construction (see Appendix 6.3 for details). The results from this exercise also concur with our understanding of the discrepant

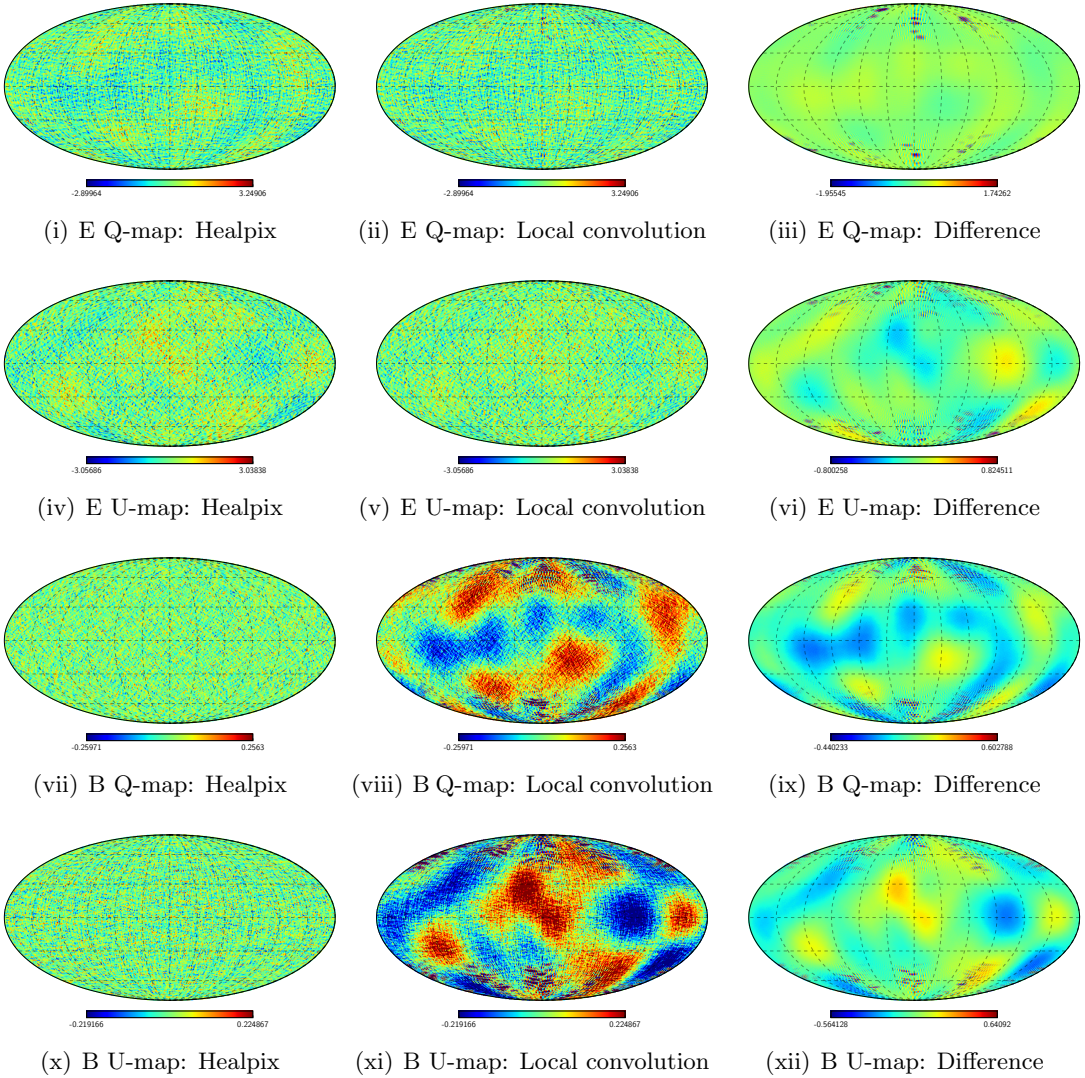


Figure 6. The top two rows depict the Stokes Q & U maps respectively corresponding to E mode of polarization while the bottom two rows depict the Stokes Q & U maps respectively corresponding to the B modes of polarization. *Left:* Stokes Maps derived using Healpix. *Middle:* Stokes maps derived using local convolution with $r_{\text{cutoff}} = 2\beta_o$. *Right:* Difference between the maps derived using the two different methods.

behaviour for the B-mode spectrum.

4.2 Separating Stokes Q & U maps corresponding to E & B modes of polarization

In this section we present the results of evaluating the local convolution given in Eq. (3.21), to decompose the total Stokes Q and U parameters into those correspond to the E modes and B modes of polarization respectively. We reiterate that this procedure uses real space operation on the total Stokes Q and U maps and does not go through the process of constructing the E and B modes as is usually the case. The resultant Stokes Q and U maps corresponding to the E mode are depicted in the first two rows while those corresponding to B modes are

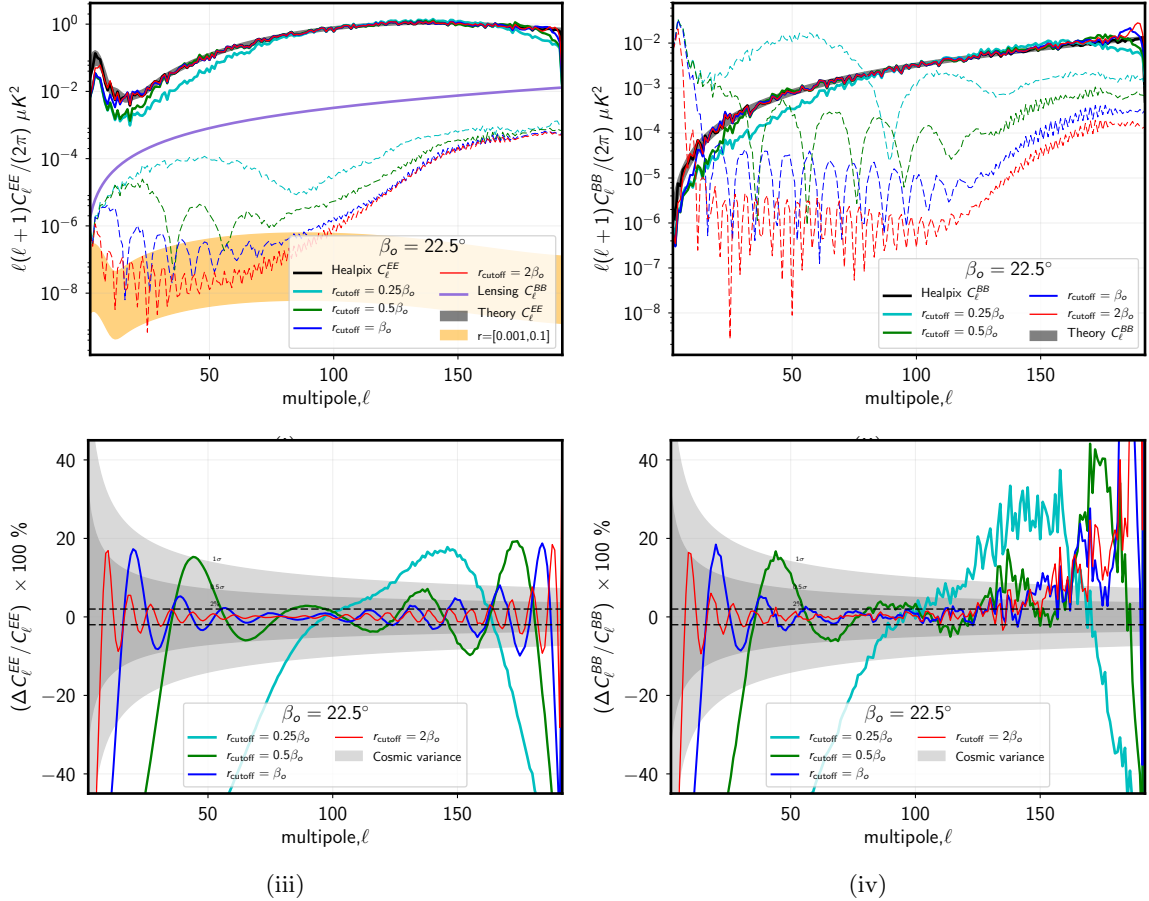


Figure 7. *Top:* The thick lines in the figure on left depicts the E mode spectra derived from pure E Stokes Q and U maps derived using different radial cutoffs, while the thin lines depict the residual B mode power. The figure on the right depict the same except that the thick lines now depict the B mode spectra while the thin lines show the residual E mode power. *Bottom:* The figure on the left and right depict the difference between the reference spectra and those derived from local convolution maps for different r_{cutoff} imposed on the convolution. In all the panels the color of the lines indicate the radial cutoff as indicated by the legend and the gray band marks the cosmic variance around the fiducial spectra.

shown in the final two rows of Fig. 6. The local convolution maps depicted in this figure are computed using a radial cutoff of $r_{\text{cutoff}} = 2\beta_o$. Note that similar to observations of the previous section, the maps derived via local real space convolutions, suffer from having relatively higher error in the polar caps, while the differences in the band around the equator are smaller and dominated by large scale modes. Next we compute the E and B mode spectra from the set of Stokes maps constructed using local convolutions with different r_{cutoff} . Note that for this exercise we use the standard Healpix routines for computing the spectra from the Stokes maps. The spectra derived from these local convolution maps and their difference with respect to the reference spectra are depicted in Fig. 7. The observations are similar to that made in the previous section: the difference with respect to the reference spectra reduce on increasing the radial cutoff and reach 2% levels at most multipoles for the maximum radial $r_{\text{cutoff}} = 2\beta_o$ used in this analysis. In particular here we note that the B-mode residue

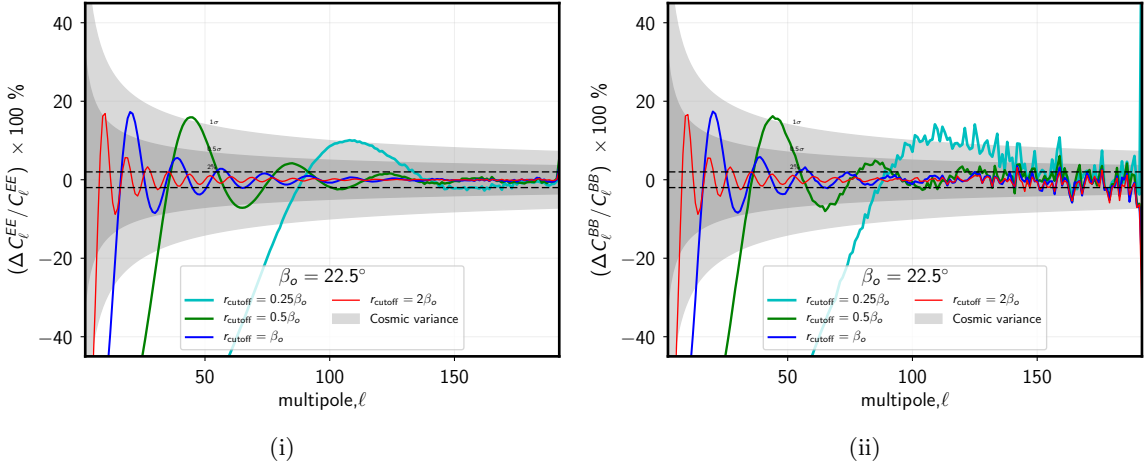


Figure 8. This figure depicts the same as the bottom panel of Fig. 7. The Stokes Q and U maps corresponding to E and B modes used in this analysis are constructed using the following relations: $[Q, U]_E = [Q, U] - [Q, U]_{Local}^B$; $[Q, U]_B = [Q, U] - [Q, U]_{Local}^E$.

in the Stokes Q & U maps corresponding to E-modes is much smaller as compared to the E-mode residue in the Stokes Q & U maps computed for the B-modes of polarization. At all multipoles the B-mode residual power is below the lensing B-modes. The E-mode residual power at low multipoles is almost fully intact.

Motivated by these observations we also compute the Stokes Q & U maps corresponding to B-modes of polarization by simply subtracting the Stokes Q & U maps corresponding to E-mode from the total Stokes Q & U maps. For completeness we also compute the Stokes Q & U maps corresponding to E-mode in an analogous manner. We carry out a spectral study on these Stokes Q & U maps corresponding to E & B modes, computed using this alternate method. The results of the spectral analysis are summarized in Fig. 8. We observe that the the low multipole spectral behavior is not affected by this alternate construction of pure Stokes Q & U maps. The high multipole behavior is significantly altered as can be seen by comparing Fig. 8 with lower panels of Fig. 7. The relative percentage difference with respect to the reference spectra is seen to lie well within 2% error for sufficiently high multipoles for all radial cutoff r_{cutoff} .

4.3 Multipole filtering using spatial convolutions

In this section we construct radial kernels which result in the desired multipole filtering, which can be achieved by simply controlling the ℓ_{\min} & ℓ_{\max} arguments of the functions $f(\beta, \ell_{\min}, \ell_{\max})$ and $\pm_2 f(\beta, \ell_{\min}, \ell_{\max})$. We reiterate that only the radial part of the convolution kernel encodes the multipole information, while the azimuthal part of the kernel is independent of multipoles. As seen in the previous sections, using local convolution methods to separate E and B modes does not allow the recovery of large scale modes. This can be understood as occurring due to the following reason: localizing the convolution kernel by introducing a radial cut off, progressively reduces the overlap of the kernels for pixels on increasing the separation between them. The overlap begins to significantly drop when angular distances are larger than r_{cutoff} and reaches a null at a separation of $2r_{\text{cutoff}}$. Owing to this overlap reduction, the pixels at large separation in the constructed maps have a re-

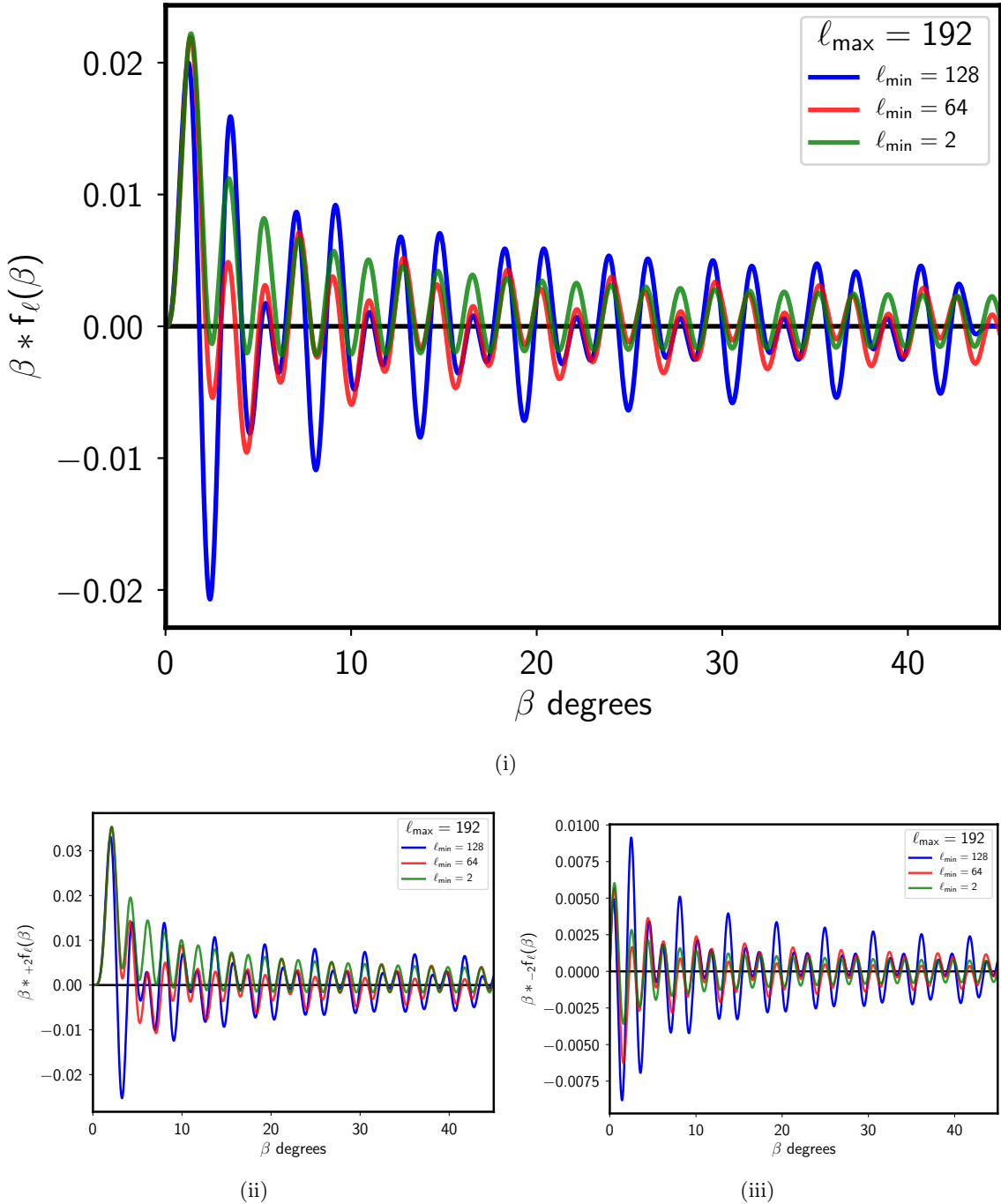


Figure 9. This figure depicts the all the radial kernels evaluated for different multipole filters. In the filtered kernels presented here, only ℓ_{min} has been altered while the maximum multipole is held fixed at $\ell_{\text{max}} = 192$. The kernels have been multiplied by a factor of the argument β to highlight the differences in the kernel at large angular separations β .

duced correlation, specifically $C(\theta > 2r_{\text{cutoff}}) = 0$. This motivates the construction of high pass filters especially while working with local convolution maps. \Rightarrow This should results in systematically lower power on large angular scales. This is observed for E mode spectra, but

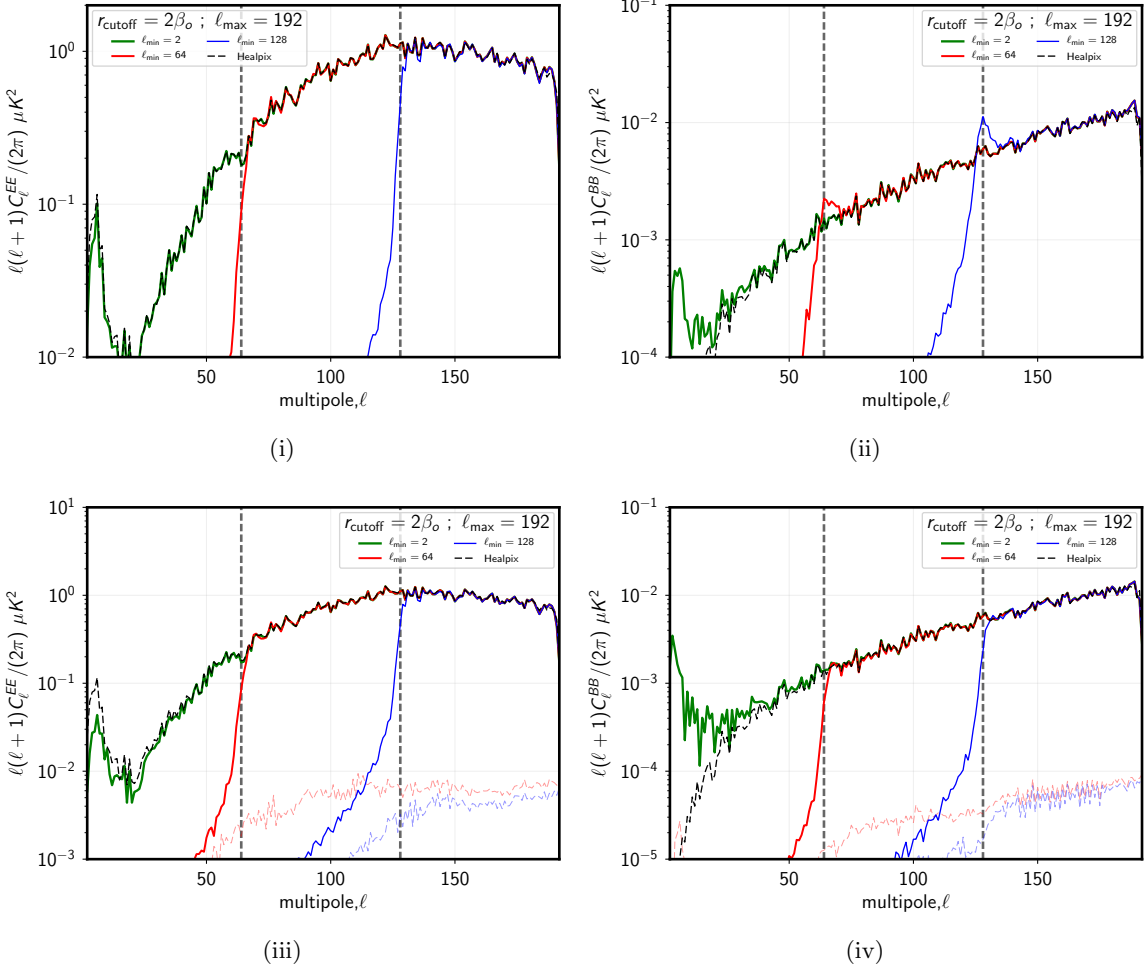


Figure 10. The top left and right panels depict the spectra for E and B modes respectively, where each panel shows the spectra derived from filtered E & B maps computed using local convolutions. The bottom left and right panels depict the same for spectra derived from $[Q, U]_E$ and $[Q, U]_B$ maps computed using local convolutions. The thin dashed lines in the bottom panels depict the residual power in the orthogonal modes. The vertical gray lines mark the low multipole cut off corresponding to $\ell_{min} = 64$ and $\ell_{min} = 128$. All local convolution have been performed with $r_{cutoff} = 2\beta_o$.

not quiet for B. Why is that ?. We construct radial filters with three different low multipole cut-offs: $\ell_{min} = 2, 64 \& 128$ which are depicted in Fig. 9. The kernels have been purposefully multiplied by a factor of the angular distance β to highlight the differences in the radial kernels for different multipole cut-offs.

We use these different radial kernels to perform local convolutions on the simulated polarization maps. We use the same radial cut off: $r_{cutoff} = 2\beta_o$ for all the different filters, where $\beta_o = 22.5^\circ$. The spectra from the filtered maps so constructed are depicted in Fig. 10. Through these results we demonstrate how we can alter the radial part of the convolution kernels to get maps with the desired multipole filtering. \Rightarrow What do you have to say about the jump in power for the B mode spectra at the low multipole cutoff, derived from filtered B maps ?

4.4 Application to Planck 353 Ghz polarization maps

In this section we apply the local convolution estimator for E and B mode maps on Planck 353 GHz polarization data. To work with our local convolution method, we reduce the resolution of the map to $N_{side} = 128$ using the Healpix `ud_grade` function. We use a high pass filter which retains modes in the multipole range $\ell = [50, 256]$. The non-locality parameter given $\ell_{\max} = 256$ is $\beta_o = 17^\circ$. We estimate the local E and B mode maps by performing local convolutions for a set of radial cut-offs: $r_{\text{cutoff}} = \beta_o, 0.5\beta_o, 0.25\beta_o$. We do not use any mask while carrying out this analysis. The resultant E and B mode maps are depicted in Fig. 11.

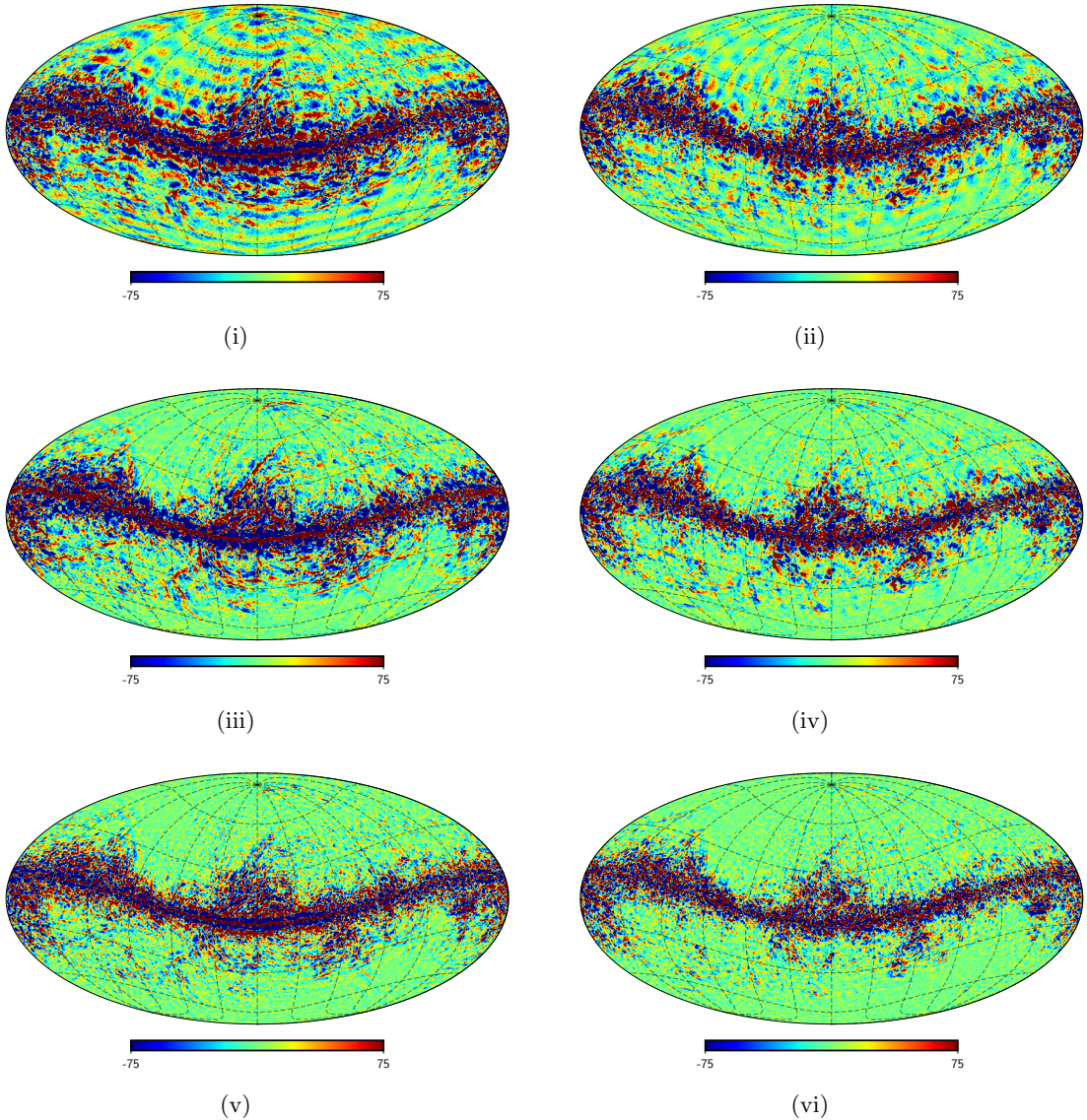
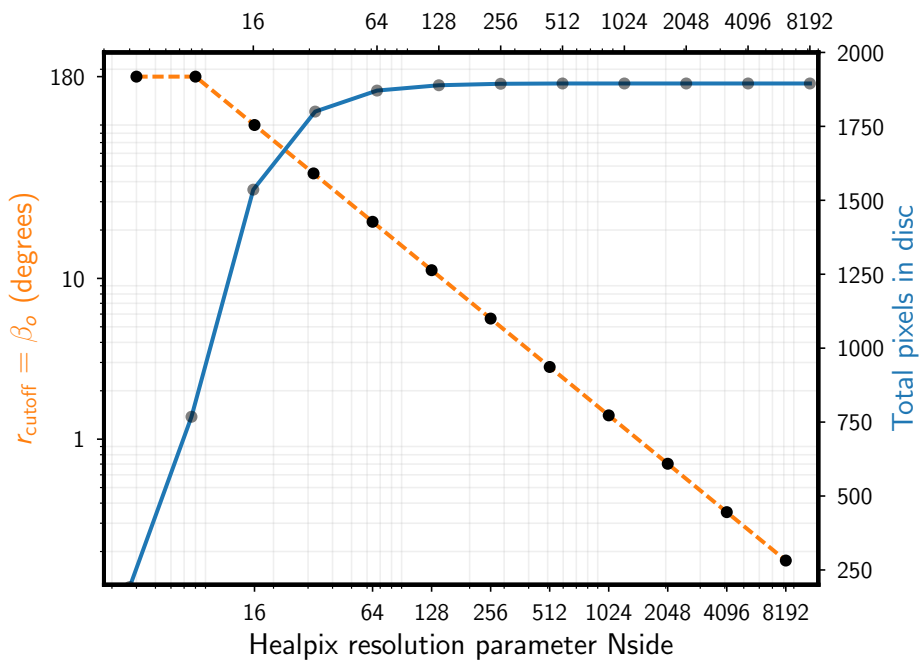


Figure 11.

4.5 Scaling and future prospects



(i)

Figure 12. The red dashed curve depicts the how β_o changes as a function of the Healpix resolution parameter N_{side} assuming that the maximum multipole accessible in the map is given by $\ell_{\text{max}} = 3 * N_{\text{side}}$. The blue solid curve depicts the number of surrounding pixel that will need to be accessed to carry out the convolution on Stokes Q & U maps to infer the value of the scalar fields E & B at the central pixel.

5 Discussion

- Many CMB experiments cannot access the large angle modes due to limited sky coverage. Often the large angle analysis is deal with in pixel space owing to the non-Gaussianity of the likelihood functions. With all these as motivations we study how the radial filters are modified by removing the large scale modes. We try to understand how removing large scale modes effects the locality of the E and B map estimators. We demonstrate that it is possible to get filtered maps by using the modifying the radial filter.
- We have derived the real space kernels for translating Stokes parameters Q & U to scalars E & B and vice versa. We have also derived real space kernels which allow for direct separation of Stokes Q & U parameters without having to first evaluate the scalar field E & B.
- These kernels quantify the non-locality of the E and B fields. We have introduced the non-locality parameter β_0 which provides a quantitative measure of the non-locality of these fields.
- Studying these real space kernels reveals that its the radial part of the kernel which knows about the band limit of the experiment. Motivation for defining radially compact kernels. We have demonstrated that using the radially compact kernels does not bias the spectral information on intermediate angular scales.
- Small field experiments like BICEP implement such radial cut offs due to limited survey area.
- Using in conjunction with FEBECOP [5] like schemes to directly infer E and B mode maps from raw maps.
- *Total convolution methods:* Since the convolution kernels can be thought of as effective beams for polarization maps, it may be possible to use total convolution methods to construct E and B mode maps.
- Separate Q and U maps for E and B: We have presented kernels which allow for decomposition of the total Stokes Q and U parameters to those corresponding to E and B modes. This could be potentially interesting, since one can now work with E and B modes foregrounds and their separations separately. \Rightarrow **But is there an issue with doing this in the standard method which involves going through the process of generating E and B modes ?**
- *Mask leakages* can be understood as arising from improper sine quadrupole and cosine quadrupole transforms on rings with holes in them due to masking. For the global mask (no point sources), by using a radially compact kernel with some β_0 , the pixels which are at a angular distance β_0 from the edges of the mask have unbiased estimates of the scalar fields E and B.
- The difference between the spectra derived from the local convolution maps and the reference spectra follow a definite pattern and maybe it possible to model this difference and correct for it. For this purpose one will have to model the two point correlation function for the E and B fields in terms of the Stokes Q and U maps.

- Poor sensitivity to large scale modes as the local estimated maps do no carry information from pixel which are further away than the radial cutoff. This should cause a compromise on spectral estimates of low multipoles, which correspond to large angular scales, much larger than radial cutoff.
- Cluster polarization will be measurable with future CMB experiments. These local estimators can be used to evaluate the local scalar modes of polarization.
- We have not addressed the E to B leakage issue in this work.

6 Appendix

6.1 Mathematical properties of spin spherical harmonics

The sum over m index of product of two spherical harmonic functions of spin s_1 and s_2 respectively, is given by the following expression [4],

$$\sum_m {}_{s_1}Y_{\ell m}^*(\hat{n}_i) {}_{s_2}Y_{\ell m}(\hat{n}_j) = \sqrt{\frac{2\ell+1}{4\pi}} {}_{s_2}Y_\ell^{-s_1}(\beta, \alpha)e^{-is_2\gamma}, \quad (6.1)$$

where α , β & γ correspond to the Euler angles that specify the rotation matrix which transforms the local cartesian coordinates defined at \hat{n}_i such that it aligns with the local cartesian coordinate system at \hat{n}_j .

The spin spherical harmonics satisfy the following orthogonality relations,

$$\int_s Y_{\ell m}(\hat{n}) {}_s Y_{\ell' m'}^*(\hat{n}) d\Omega = \delta_{\ell\ell'} \delta_{mm'}, \quad (6.2)$$

where s denotes the spin of the spherical harmonic coefficients. The numerical validity of Eq. (6.2) is only limited by the rate at which these functions are sampled on the sphere and hence this identity can be made arbitrarily accurate by choosing a sufficiently high sampling rate.

The spin spherical harmonic functions satisfy the following completeness relation,

$$\sum_{\ell m} {}_s Y_{\ell m}(\hat{n}_i) {}_s Y_{\ell m}^*(\hat{n}_j) = \delta(\hat{n}_i - \hat{n}_j), \quad (6.3)$$

Note that the numerical validity of Eq. (6.4) is strictly true only when the sums over the indices (ℓ, m) run to infinity. This is never true in practice, since the measured data invariable are band limited owing to the finite resolution of the experiments. Hence this relation is only approximately true and in more realistic scenario takes up the following function form,

$$\begin{aligned} \sum_{\ell=\ell_{\min}, m}^{\ell_{\max}} {}_{s_1}Y_{\ell m}^*(\hat{n}_i) {}_{s_2}Y_{\ell m}(\hat{n}_j) &\approx \delta(\hat{n}_i - \hat{n}_j), \\ &= \sum_{\ell=\ell_{\min}}^{\ell_{\max}} \sqrt{\frac{2\ell+1}{4\pi}} {}_{s_2}Y_\ell^{-s_1}(\beta, \alpha)e^{-is_2\gamma}, \end{aligned} \quad (6.4)$$

where α, β & γ are the Euler angles relating the two directions \hat{n}_i and \hat{n}_j . A specific case of this function with $(s = 2, \ell_{\min} = 2, \ell_{\max} = 96)$ is depicted in the last two columns of Fig. 2.

6.2 Asymptotic forms for the functions $\pm f_\ell(\beta)$

The functions $\pm f_\ell(\beta)$ need to be evaluated close to $\beta = 0$ and $\beta = \pi$. Close to these values we cannot evaluate these functions using the relation given in Eq. (3.20), owing to the inverse $\sin(\beta)$ dependence of a number of terms. To overcome this issue, we use the asymptotic form of the Legendre polynomials as $\beta \rightarrow 0$,

$$P_\ell^2(\cos \beta) = \sin^2(\beta) \frac{(\ell+2)!}{8(\ell-2)!}. \quad (6.5)$$

Using the above limiting form, the functions $\pm f_\ell(\beta)$ reduce to the following equations,

$$\lim_{\beta \rightarrow 0} \pm f_\ell(\beta) = \frac{1}{4} \sqrt{\frac{2\ell+1}{4\pi}} \left\{ - \left[(\ell-4) + \frac{1}{2}\ell(\ell-1) \sin^2(\beta) \pm 2(\ell-1) \cos(\beta) \right] + [(\ell-2) \cos(\beta) \pm 2(\ell-2)] \right\}. \quad (6.6)$$

Using the parity property of the associate Legendre polynomials: $P_\ell^m(-x) = (-1)^{\ell+m} P_\ell^m(x)$, the asymptotic form for the functions $\pm f_\ell(\beta)$ in the limit $\beta \rightarrow \pi$ are given by the following equations,

$$\lim_{\beta \rightarrow \pi} \pm f_\ell(\beta) = \frac{1}{4} \sqrt{\frac{2\ell+1}{4\pi}} \left\{ - \left[(\ell-4) + \frac{1}{2}\ell(\ell-1) \sin^2(\beta) \pm 2(\ell-1) \cos(\beta) \right] (-1)^\ell + [(\ell-2) \cos(\beta) \pm 2(\ell-2)] (-1)^{\ell-1} \right\}. \quad (6.7)$$

We use these asymptotic forms for $\pm f_\ell(\beta)$ to evaluate the radial kernel close to the poles.

6.3 Convolution error

Here we assess error in the simple integeration scheme used in our python script. To estimate the error, we use the Healpix integration scheme as the reference. The spatially local convolutions suggested in this work can be carried out using Healpix via the following algorithm: (i) Generate a disc mask of radius r_{cutoff} around a pixel with index “i”. (ii) Apply the mask on the Stokes Q & U maps and evaluate the E & B maps using standard Healpix functions. (iii) Store the E & B field values evaluated at the pixel with index “i” (the center of the disc mask), while rejecting the fields constructed at other pixels in the mask. (iv) Repeat this process at all pixels to generate a map of the scalar fields E & B. This scheme is mathematical identical to our implementation of carrying out the convolution integrals over spatially local regions. In the above proposed algorithm the locality is enforced by the disc mask. However note that evaluating this scheme using Healpix is extremely inefficient since it effectively involves translating Npix Stokes Q & U maps to scalar E & B maps. The computational cost of carrying out this operation using Healpix grows quickly with the resolution parameter Nside. For the results presented here we work with Healpix maps simulated at a resolution of Nside=64.

We evaluate the E & B maps using three different methods, using our simple Python implementation of the local convolutions, the equivalent scheme using Healpix as described above and the full sky Healpix evaluation (which we use to evaluate the reference spectra). The relative percentage differences between the spectra derived from maps using the local methods and the reference spectra are depicted in Fig. 13. Note that the error on the E mode spectrum derived from maps constructed using the two different local convolution methods nearly match each other. However for the B-mode spectrum, the error on the spectrum derived from our python implementation is significantly larger as compared to the error on the spectrum derived from the local Healpix convolution method. This indicated the fact that Healpix convolution has a better accuracy as compared our implementation. More important to note here is the fact that the error on the spectra from locally evaluated E and B mode maps are nearly equal to each other, as can be seen by comparing the green curves in the left and and right panels of Fig. 13.

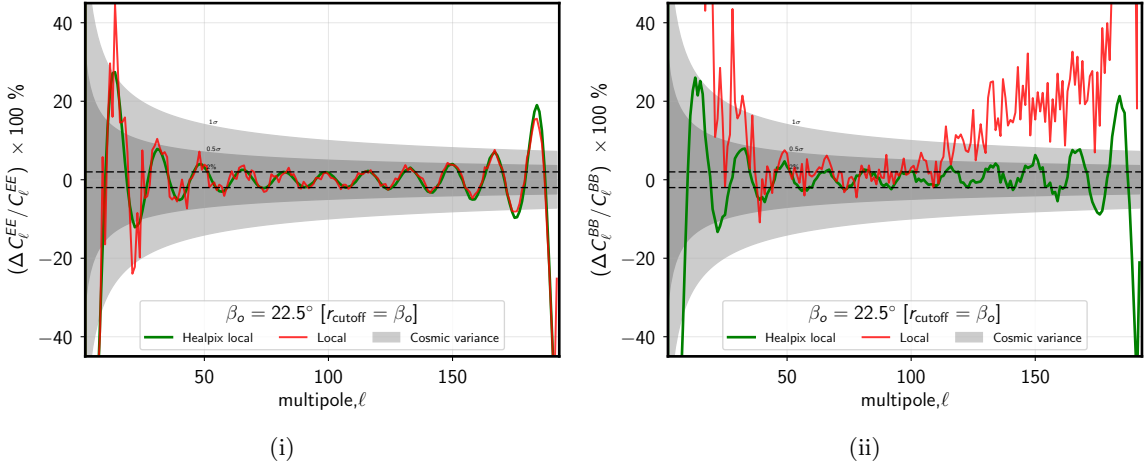


Figure 13. The figure on the left and right depict the relative percentage difference between spectra derived from local convolution estimates of E & B map and the reference spectra derived from full sky Healpix evaluations. The green curves depict the results from local E & B maps evaluated using local Healpix operations while the red curve shows the same for the scalar maps derived using our python script. The gray band indicates the scatter expected due to cosmic variance, the lighter shade corresponding to 1σ and the darker shade to 0.5σ . **The cosmic variance band does not account for the non-gaussian distribution, which is particularly relevant at the low multipoles.**

6.4 Local convolution kernels using standing Healpix routines

Healpix uses Euler angles given in the z-y-z convention in contrast to the Euler angle definitions given in Sec. ?? which are in z-y1-z2 convention. The two set of Euler angles are related by the following relations $(\alpha, \beta, \gamma)_{z-y-z} = (\gamma, \beta, \alpha)_{z-y1-z2}$ [4]. We know the exact form of the harmonic coefficients for the kernels when they are centered around the north pole. Therefore the kernels centered around any arbitrary Healpix pixel \hat{n}_i can be calculated by simply rotating these harmonic coefficients by the Euler angles $(0, \theta_i, \phi_i)_{z-y-z}$ and synthesizing the kernel by evaluating the harmonic sum.

6.5 The correlation function and radial cut offs.

6.6 Explaining the oscillations in spectra and recovering the true spectra

The radial part of the convolution kernel which translates Stokes parameters Q & U to scalar E & B is given by the following expression,

$$R_{QU \leftrightarrow EB}(\beta) = R(\beta) = \sum_{\ell=\ell_{\min}}^{\ell_{\max}} \sqrt{\frac{2\ell+1}{4\pi} \frac{(\ell-2)!}{(\ell+2)!}} P_\ell^2(\cos \beta), \quad (6.8)$$

where P_ℓ^2 are the associated Legendre polynomials. Note that the form of the radial kernel remains unchanged for the forward \bar{O} and the inverse operators \bar{O}^{-1} .

While translating from Stokes Q & U parameters which form a spin-2 field to spin-0 scalars E & B, the azimuthal part of the convolution is restricted to have the form $e^{-i2\phi}$. The only freedom is to choose the radial part of the convolution kernel. It is possible to generalize the form of the radial kernel by introducing the following redefinition,

$$G_{QU \rightarrow EB}(\beta) = G(\beta) = \sum_{\ell=\ell_{\min}}^{\ell_{\max}} b_\ell \sqrt{\frac{2\ell+1}{4\pi} \frac{(\ell-2)!}{(\ell+2)!}} P_\ell^2(\cos \beta), \quad (6.9)$$

where b_ℓ encodes the desired changes to the radial function. This radial function now defines the modified forward operator \bar{O}' . Since we require the following property: $\bar{O}'\bar{O}'^{-1} = I$ to hold true, the inverse operator cannot have the same form for the radial function. Demanding $\bar{O}'\bar{O}'^{-1} = I$ to hold true it can be shown that the radial part of the inverse operator has to take up the following form,

$$G_{EB \rightarrow QU}(\beta) = G^{-1}(\beta) = \sum_{\ell=\ell_{\min}}^{\ell_{\max}} b_\ell^{-1} \sqrt{\frac{2\ell+1}{4\pi} \frac{(\ell-2)!}{(\ell+2)!}} P_\ell^2(\cos \beta), \quad (6.10)$$

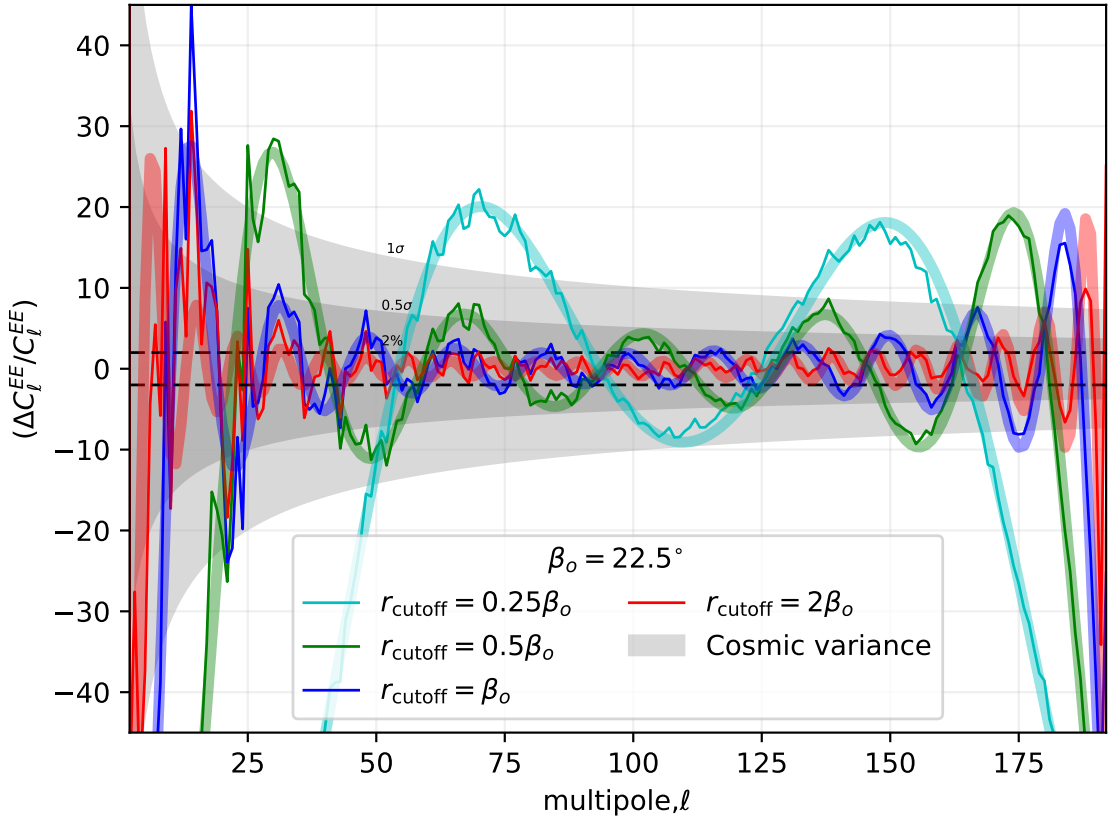
where b_ℓ is the same multipole function introduced in Eq. (6.9). Therefore for the forward and backward operators to be well behaved we are restricted in choosing multipole functions b_ℓ such that its inverse is well defined. If this constraint is overlooked, the ability to transform back and forth between the Stokes parameters and the scalar representation of the CMB polarization field is compromised. Given this general definition for the radial function $G(\beta)$, note that the radial function $R(\beta)$ is just a special case formed by making the choice $b_\ell = 1$. Note that for this choice the inverse of the multipole function is itself $b_\ell^{-1} = b_\ell$ and therefore $G^{-1}(\beta) = G(\beta)$.

While modifying the radial function, it makes more sense to make a choice on the real space function $G(\beta)$ instead of choosing the multipole function b_ℓ . We use the orthogonality property of associated Legendre polynomials to express the multipole function b_ℓ as,

$$b_\ell = 2\pi \sqrt{\frac{(\ell-2)!}{(\ell+2)!}} \int_0^\pi G(\beta) P_\ell^2(\cos \beta) d\cos \beta, \quad (6.11)$$

where we have used the orthonormality property of the associated Legendre polynomials to arrive at the above equation. Note that once the choice of $G(\beta)$ is made, the inverse function $G^{-1}(\beta)$ is automatically defined by the forward relation given in Eq. (6.10).

In Sec. 4.1 we constructed localized convolution kernels by multiplying $R(\beta)$ with an apodized version of the step function $\theta_{\text{apo}}(r_{\text{cutoff}})$. The oscillation seen in the spectra in Fig. 5 can be explained to be due to this effective beam characterized by b_ℓ^2 operating on the



(i)

Figure 14. The thin lines depicts the same spectral differences as those seen in Fig. 5, while the thick lines of the corresponding color depict the function $b_\ell^2 - 1$ as derived from evaluating Eq. (6.12) for different r_{cutoff}

power spectra. The effective beam can be evaluated by computing the multipole function b_ℓ as follows,

$$b_\ell = 2\pi \sqrt{\frac{(\ell-2)!}{(\ell+2)!}} \int_0^{r_{\text{cutoff}}} R(\beta) \theta_{\text{apo}}(r_{\text{cutoff}}) P_\ell^2(\cos \beta) d\cos \beta , \quad (6.12)$$

where the upper limit of the integration is set to r_{cutoff} since the function $\theta_{\text{apo}}(r_{\text{cutoff}})$ vanishes for $\beta > r_{\text{cutoff}}$. The function $b_\ell^2 - 1$ matches the oscillation seen in Fig. 5 as seen in Fig. 14 where the two results have been over plotted. The apodized step function in this case transition from 1 at $\beta < r_{\text{cutoff}} - w$ to 0 at r_{cutoff} over a width $w = 3^\circ$ with a cosine squared profile .

References

- [1] M. Zaldarriaga, *The nature of the E-B decomposition of CMB polarization*, *Phys. Rev. D* **64** (jun, 2001) 103001, [[0106174](#)].
- [2] M. Kamionkowski, A. Kosowsky and A. Stebbins, *Statistics of cosmic microwave background polarization*, *Phys. Rev. D* **55** (1997) 7368–7388, [[9611125](#)].
- [3] J. N. Goldberg, A. J. Macfarlane, E. T. Newman, F. Rohrlich and E. C. G. Sudarshan, *Spin-s Spherical Harmonics and \eth*, *J. Math. Phys.* **8** (nov, 1967) 2155.
- [4] D. A. Varshalovich, A. N. Moskalev and V. K. Khersonskii, *Quantum Theory of Angular Momentum* (World Scientific). World Scientific, 1988.
- [5] S. Mitra, G. Rocha, K. M. Górski, K. M. Huffenberger, H. K. Eriksen, M. a. J. Ashdown et al., *FAST PIXEL SPACE CONVOLUTION FOR COSMIC MICROWAVE BACKGROUND SURVEYS WITH ASYMMETRIC BEAMS AND COMPLEX SCAN STRATEGIES: FEBECoP*, *Astrophys. J. Suppl. Ser.* **193** (mar, 2011) 5, [[1005.1929](#)].